Impedance of nanocapacitors from molecular simulations to understand the dynamics of confined electrolytes

Giovanni Pireddu, Connie J Fairchild, Samuel P Niblett, Stephen J Cox, Benjamin Rotenberg

Impedance of nanocapacitors from molecular simulations to understand the dynamics of confined electrolytes

Giovanni Pireddu,[†] Connie J. Fairchild,[‡] Samuel P. Niblett,[‡] Stephen J. Cox,[‡] and Benjamin Rotenberg[*,†,¶]

†*Sorbonne Université, CNRS, Physico-chimie des Électrolytes et Nanosystèmes Interfaciaux, PHENIX, F-75005 Paris*

‡*Yusuf Hamied Department of Chemistry, University of Cambridge, Cambridge CB2 1EW, United Kingdom*

¶*Réseau sur le Stockage Electrochimique de l'Energie (RS2E), FR CNRS 3459, 80039 Amiens Cedex, France*

E-mail: benjamin.rotenberg@sorbonne-universite.fr

Abstract

Nanoelectrochemical devices have become a promising candidate technology across various applications, including sensing and energy storage, and provide new platforms for studying fundamental properties of electrode/electrolyte interfaces. In this work, we employ constant-potential molecular dynamics simulations to investigate the impedance of gold-aqueous electrolyte nanocapacitors, exploiting a recently-introduced fluctuation-dissipation relation. In particular, we relate the frequency-dependent impedance of these nanocapacitors to the complex conductivity of the bulk electrolyte in different regimes, and use this connection to design simple but accurate equivalent circuit

models. We show that the electrode/electrolyte interfacial contribution is essentially capacitive and that the electrolyte response is bulk-like even when the interelectrode distance is only a few nanometers, provided that the latter is sufficiently large compared to the Debye screening length. We extensively compare our simulation results with spectroscopy experiments and predictions from analytical theories. In contrast to experiments, direct access in simulations to the ionic and solvent contributions to the polarization allows us to highlight their significant and persistent anticorrelation and to investigate the microscopic origin of the timescales observed in the impedance spectrum. This work opens avenues for the molecular interpretation of impedance measurements, and offers valuable contributions for future developments of accurate coarse-grained representations of confined electrolytes.

Introduction

In recent decades, fueled by technological advances, the miniaturization of electrochemical devices has made tremendous progress. In this context, micro- and nanogap devices have demonstrated peculiar properties and promising performance in nanofluidics,[1,2] sensing,[3–5] as well as energy storage and conversion applications.[6,7] Beyond their technological importance, nanoelectrochemical devices serve as valuable platforms for acquiring fundamental insights into solid-liquid interfaces,[8,9] highlighting how microscopic phenomena can impact macroscopic properties. For instance, nanofluidic experiments[10] (later corroborated by theoretical and computational studies[11,12]) have shown how friction can be massively modified at water/carbon interfaces because of the coupling of electronic and dielectric fluctuations between the solid and the liquid. Recent studies have also focused on the dielectric properties of confined liquids between planar walls, revealing the influence of the inter-plane separation on the static dielectric response[13–15] and its anisotropy.[16–19]

In electrochemical devices, and in particular for capacitors, the dynamical dielectric/electrical response is assessed through electrochemical impedance spectroscopy (EIS) experiments.[20–22]

Here, the impedance $Z(\omega)$ [or equivalently the admittance $Y(\omega) = 1/Z(\omega)$] quantifies the system's electric current response $I(\omega)$ to an oscillating voltage $\Delta\Psi(\omega)$, under linear response conditions. EIS results are commonly interpreted through equivalent circuit (EC) models,[23,24] which are fitted to the experimental data to extract parameters such as the electrical resistance R, capacitance C, and, more broadly, the distribution of relevant time scales governing polarization and charge transport.[25] One of the most commonly used EC models is the transmission line model (TLM),[26–29] which is employed to model the charging dynamics of capacitors with porous electrodes. Despite their popularity, the physical interpretation of such representations is not always straightforward and has led to long-standing debates (see, e.g., Ref. 30). For this reason, coupling experiments with theoretical and computational investigations is crucial to elucidate the physical mechanisms behind a given electrochemical signal.

Popular approaches to model the dynamical response of capacitors include analytic mean-field theories[31–35] and numerical simulations at the mesoscale.[36,37] The tractability of such approaches, however, relies on strong assumptions that often neglect important molecular details. In recent years, molecular simulations have proven a powerful tool to investigate the electrode-electrolyte interface that retain details about relevant molecular correlations.[38–41] In particular, classical constant-potential molecular dynamics (MD) simulations have been extensively used to uncover the microscopic mechanisms that underlie macroscopic properties of electrochemical devices, such as supercapacitors.[42–45] In this kind of simulation, the electrode charges fluctuate in response to changes in the electrolyte configuration, subject to the constraints of constant applied potential and global neutrality.[46–48]

The dynamical behavior of the total charge $Q(t)$ of an electrode, which fluctuates in the constant-potential ensemble, provides a means to obtain important electrochemical information about the system. For example, following the classic approach of Johnson and Nyquist,[49,50] in fact anticipated in 1912 by De Haas-Lorentz in her PhD thesis,[51] one can use the equilibrium charge or current fluctuations to compute the electrical response of

an electrochemical system. Indeed, previous works have shown how the differential capacitance, which describes how the average electrode charge changes with applied potential $\Delta\Psi$, can be calculated from the charge fluctuations using a fluctuation-dissipation relation $C_{\text{diff}} = \partial\langle Q\rangle/\partial\Delta\Psi = \beta\langle\delta Q^2\rangle$, where brackets denote an ensemble average, $\delta Q = Q - \langle Q\rangle$ and $\beta = 1/k_{\text{B}}T$ with k_{B} the Boltzmann constant and T the temperature.[48,52,53] Furthermore, in recent work,[54] this fluctuation-dissipation relation was extended to dynamical properties, in particular, to calculate the whole impedance spectrum from the total charge autocorrelation function $\langle\delta Q(0)\delta Q(t)\rangle$ (QACF). This approach was illustrated for the case of nanocapacitors with pure water confined between electrodes.

In this work, we leverage this approach to investigate a far more challenging problem: To understand the electrochemical impedance of electrolyte solutions. Not only do the long time scales associated with ionic motion mean statistical sampling is more demanding than the pure water case, but, as we will see, differences in the underlying statistical mechanics of electrolytes vs dielectrics play an important role in interpreting the resulting impedance. For the simple aqueous electrolyte that we investigate, however, we show that a simple EC model comprising just bulk and interfacial elements is remarkably accurate in describing the simulation results. Even more surprisingly, we find that the interfacial contribution is purely capacitive, i.e., there is no measurable interfacial resistance. We also discuss the time scales of charge relaxation obtained in our MD simulations, and highlight the limitations of standard analytical theories. At the microscopic level, our simulations show that this arises from a coupling of solvent and ionic fluctuations, a feature that is only approximately taken into account in most implicit-solvent models of electrochemical response.

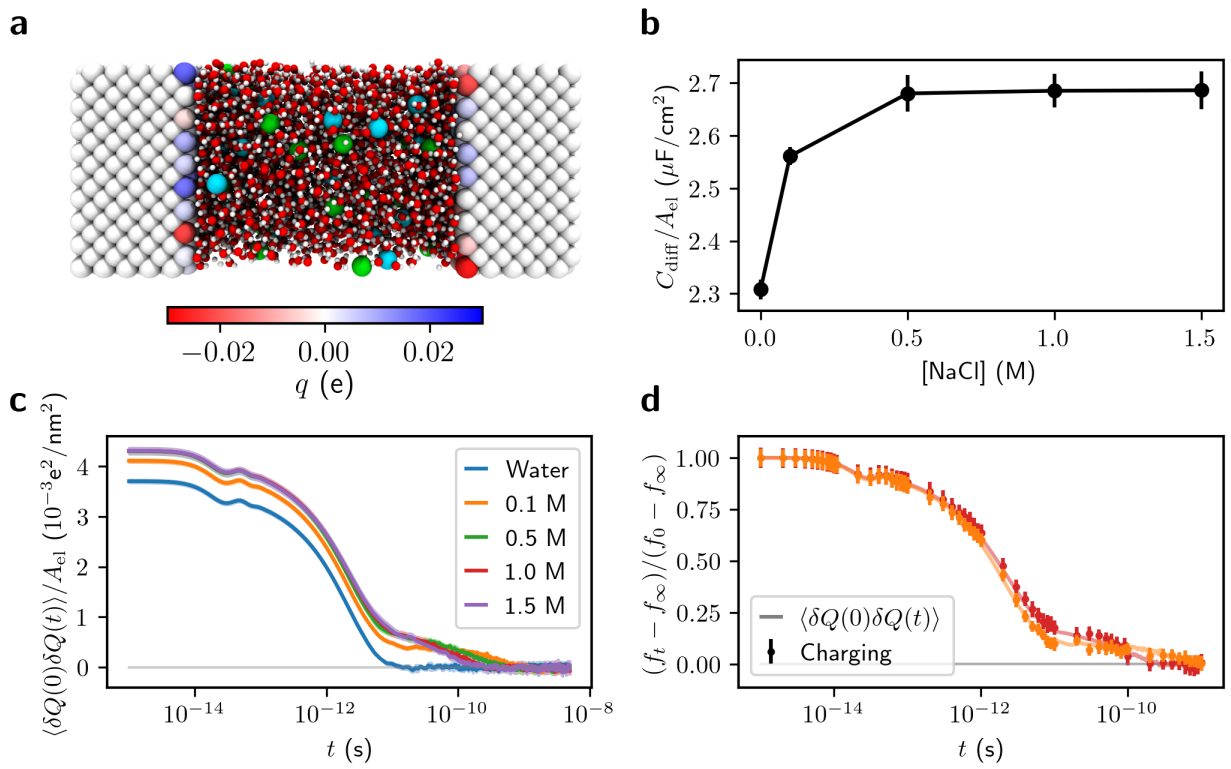

Figure 1: (a) Snapshot of the 1.0 M NaCl system, with the color of gold electrode atoms representing their instantaneous charge, as indicated by the color bar. Hydrogen, oxygen, sodium and chloride atoms are represented as white, red, cyan and green spheres, respectively. (b) Differential capacitance C_{diff} divided by the electrode area A_{el}, as a function of NaCl concentration. (c) Electrode charge autocorrelation function divided by A_{el} for the five salt concentrations we considered. (d) Comparison of the responses to a voltage change from $\Delta\Psi = 0$ to 1 V (symbols) with the equilibrium charge ACFs $\langle \delta Q(0)\delta Q(t)\rangle$, normalized as $(f(t) - f(\infty))/(f(0) - f(\infty))$, where $f(t)$ is either $Q(t)$ recorded during the charging process (symbols), or $\langle \delta Q(0)\delta Q(t)\rangle$ at equilibrium (solid lines), for the 0.1 M and 1 M systems. The uncertainty, calculated as 95% confidence intervals, is represented as error bars in panels (b) and (d), and with shaded areas in panel (c).

Results and discussion

Electrode charge dynamics and salt concentration

We consider NaCl(aq)-gold nanocapacitors at four different salt concentrations: 0.1 M, 0.5 M, 1.0 M, and 1.5 M. To emphasize the fundamental differences between electrolytes and dielectric media, we also compare to simulation results for pure water.[54] A representative snapshot for the 1 M case is shown in Figure 1(a). For each concentration, the interelec-

trode distance $d \approx 5$ nm was obtained from the average of a constant pressure simulation at atmospheric pressure and $T = 298$ K. Simulations at constant $\Delta\Psi$ (and constant volume) were performed with the fluctuating charge method, where the atomic charges on the electrode atoms are calculated self-consistently depending on the instantaneous electrolyte configuration at each simulation step.[47] The consequences of such a Born-Oppenheimer (BO) approximation on charge fluctuations and electrochemical properties have been discussed in previous works.[48,54] In addition, recent works in the context of nanoscale flow have shown how dynamical coupling between electronic degrees of freedom in a solid and dielectric fluctuations in a fluid can impact interfacial friction.[11,12] Such effects are also neglected in the BO approximation; their potential impact on (high-frequency) impedance, which depends on the specific details of how they are described, lies beyond the scope of this work. We perform two types of simulations: (i) we characterize the equilibrium fluctuations of the system with $\Delta\Psi = 0$ V; (ii) we interrogate the nonequilibrium response of the solution to a voltage step by instantaneously switching $\Delta\Psi = 0 \to 1$ V. More simulation details are provided in *Methods* and *SI Appendix*.

Figure 1(b) shows the differential capacitance, C_{diff}, estimated from the fluctuations of the total charge Q on one of the two electrodes[48,52] as a function of salt concentration. Note that these results do not account for the empty capacitor contribution $C_{\text{diff}}^{\text{empty}}$, which results from the fluctuations neglected by the BO approximation.[48] This contribution depends in particular on the distance between the electrodes and typically amounts to $\sim$10% of the BO capacitance for the systems considered in the present work. The capacitance values for the pure water and 1 M cases are in excellent agreement with recent simulation results on the same setup[55] and compare favorably with simulations performed with different force-fields.[56,57] Our results show that the presence of ions introduces a positive contribution to capacitance. However, the capacitance does not depend on the salt concentration beyond 1 M in the considered range. A similar trend was found in simulations of supercapacitors[58] and in recent impedance experiments for NaCl solutions at planar electrodes, where C_{diff}

was found to be almost constant for salt concentrations spanning six orders of magnitude.[59] Interestingly, these results are in stark contrast with the cell capacitance values predicted by Debye-Hückel (DH) theory,

$$C_{\mathrm{DH}} = \frac{1}{2} A_{\mathrm{el}} \frac{\varepsilon_0 \varepsilon_{\mathrm{w}}}{\lambda_{\mathrm{D}}}, \tag{1}$$

where A_{el} is the surface area of each electrode, ε_0 is the vacuum permittivity, ε_{w} is the permittivity of the solvent, and the Debye screening length is given by

$$\lambda_{\mathrm{D}} = \left(\frac{\varepsilon_{\mathrm{w}} \varepsilon_0 k_{\mathrm{B}} T}{e^2 \sum_\alpha c_\alpha Z_\alpha^2} \right)^{\frac{1}{2}}, \tag{2}$$

where e is the elementary charge and the sum runs over the species α with concentration c_α and valency Z_α. Using $\varepsilon_{\mathrm{w}} = 70.7$ for SPC/E water,[60] Eq. 1 predicts capacitances that are $\sim$25 to $\sim$100 times larger (at 0.1 M and 1.0 M, respectively) than the values obtained from simulations. This mismatch is not unexpected, given that DH theory implies a very simplified picture of the electrode/electrolyte interface. Furthermore, at sufficiently high salt concentrations (i.e., ≥ 0.5 M), λ_{D} becomes comparable to the ionic size, a regime where ionic correlations and molecular features of the solvent, which are neglected entirely in DH theory, are known to become important.[38,61] More sophisticated capacitance models could be used to fit MD results,[58] but this falls beyond the scope of the present work.

Fig. 1(c) shows $\langle \delta Q(0) \delta Q(t) \rangle$ for the different salt concentrations we consider. The QACFs in the presence of ions share some qualitative similarities with the pure water case. However, for finite salt concentrations, we observe an additional exponential-like slow mode with a decay rate that depends on concentration (discussed below, see also *SI Appendix* and Fig. S1). In particular, the relaxation rate of the slow mode is faster for higher salt concentrations. In the considered concentration range, it is known (and we will confirm later) that the ionic conductivity increases with salt concentration.[62] The observed long-time behavior of the QACFs therefore suggests an intuitive connection with the ionic conductivity.

The impedance that we will derive from these QACFs describes the linear response between the current and voltage. This raises the issue of the voltage range over which the response is linear. We address it by performing nonequilibrium simulations where we subject the system to a step change $\Delta\Psi = 0 \rightarrow 1$ V, and measure $Q(t)$ as it relaxes to a new equilibrium. Results for the 0.1 M and 1.0 M systems are presented in Fig. 1d, where we also compare to the predicted nonequlibrium response from the QACFs. The excellent agreement between the equilibrium and nonequilibrium results demonstrates that linear response is a valid approximation (see *SI Appendix*), at least up to $\Delta\Psi = 1$ V. This is consistent with previous results for water/gold nanocapacitors.[54] Having established this fact, we now use these QACFs to obtain the impedance.

Impedance of nanocapacitors as bulk impedance and interfacial capacitance

Confined electrolytes Following the approach used in Ref. 54 for pure water, we obtain $Z(\omega)$ from the QACF sampled at $\Delta\Psi = 0$ V. As in this previous work, and for consistency with the BO contribution to the differential capacitance (see above), we limit our analysis to the impedance contributions within the BO approximation. Figs. 2(a) and (b) report the real and imaginary parts of $Z(\omega)$, respectively. Here, to represent intensive quantities, $Z(\omega)$ is multiplied by $A_{\mathrm{el}}/d_{\mathrm{DDS}}$, where $d_{\mathrm{DDS}} = d - 2w_{\mathrm{DDS}}$ is the effective width of the confined electrolyte based on the positions of the dielectric dividing surface at each electrode/electrolyte interface.[16] Roughly speaking, w_{DDS} is the width of the vacuum layer between the first atomic plane of the electrode and the closest water molecules. In this work, we use $w_{\mathrm{DDS}} = 1.27$ Å from Ref. 54, which employed the same force field as this study (without salt).

The impedance results display some distinctive features of capacitors at low frequencies.[20] In particular, the real part $\Re[Z(\omega)]$ plateaus at $\omega \rightarrow 0$, corresponding to the total electrical resistance of each electrochemical system. For finite salt concentrations, resistance decreases with increasing salt concentration, suggesting an intuitive link with bulk conductivity, which

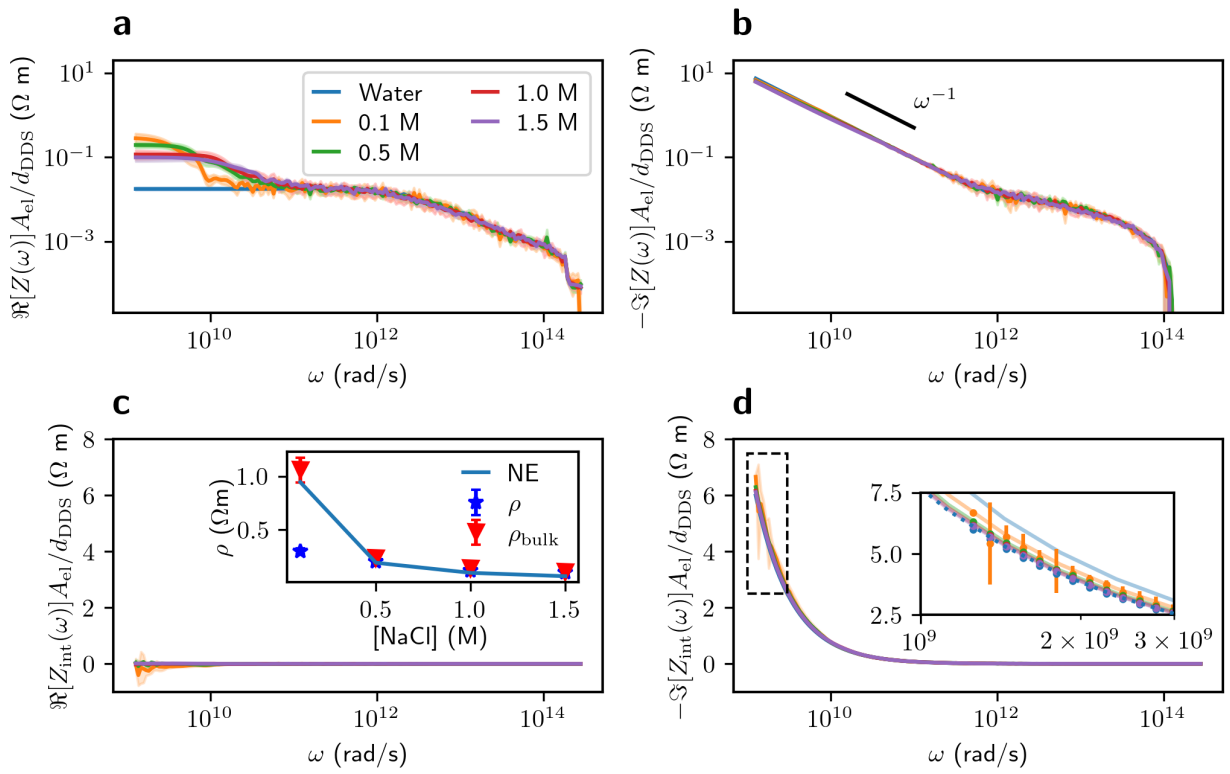

Figure 2: (a) Real and (b) imaginary parts of the total impedance $Z(\omega)$ as calculated from confined simulations for all the salt concentrations we considered, as a function of frequency. (c) Real and (d) imaginary parts of interfacial impedance $Z_{\mathrm{int}}(\omega)$. The inset in (c) shows the resistivity $\rho = \Re[Z(\omega \to 0)]A_{\mathrm{el}}/d_{\mathrm{DDS}}$, estimated as described below Eq. 9, and $\rho_{\mathrm{bulk}} = 1/\sigma_0$, with the EH and Nernst-Einstein (NE) estimates of the conductivity. The inset in (d) highlights the low frequency behavior of $\Im[Z_{\mathrm{int}}(\omega)]$, as indicated by the black dashed box in the main panel. Solid lines indicate $\Im[Z_{\mathrm{int}}(\omega)] = -1/\omega C_{\mathrm{diff}}$, and the dotted line shows $\Im[Z_{\mathrm{int}}(\omega)] = -1/\omega C_{\mathrm{w,int}}$ given by Eq. 8. Symbols show results from our molecular simulations.

will be further discussed below. Furthermore, the imaginary part $\Im[Z(\omega)]$ displays a clear ω^{-1} scaling at low frequencies, which is typical of capacitive systems. Above $\omega \gtrsim 10^{11}$ rad/s, the impedance results do not depend on salt concentration and closely resemble that for pure water. This overlap suggests that, at high frequencies, the impedance reflects the individual motion of solvent molecules and ions, which, under the concentrations we consider, is dominated by water.

The global response of the confined systems encoded in $Z(\omega)$ includes all the molecular correlations that contribute to the total polarization or charge dynamics. Intuitively, we

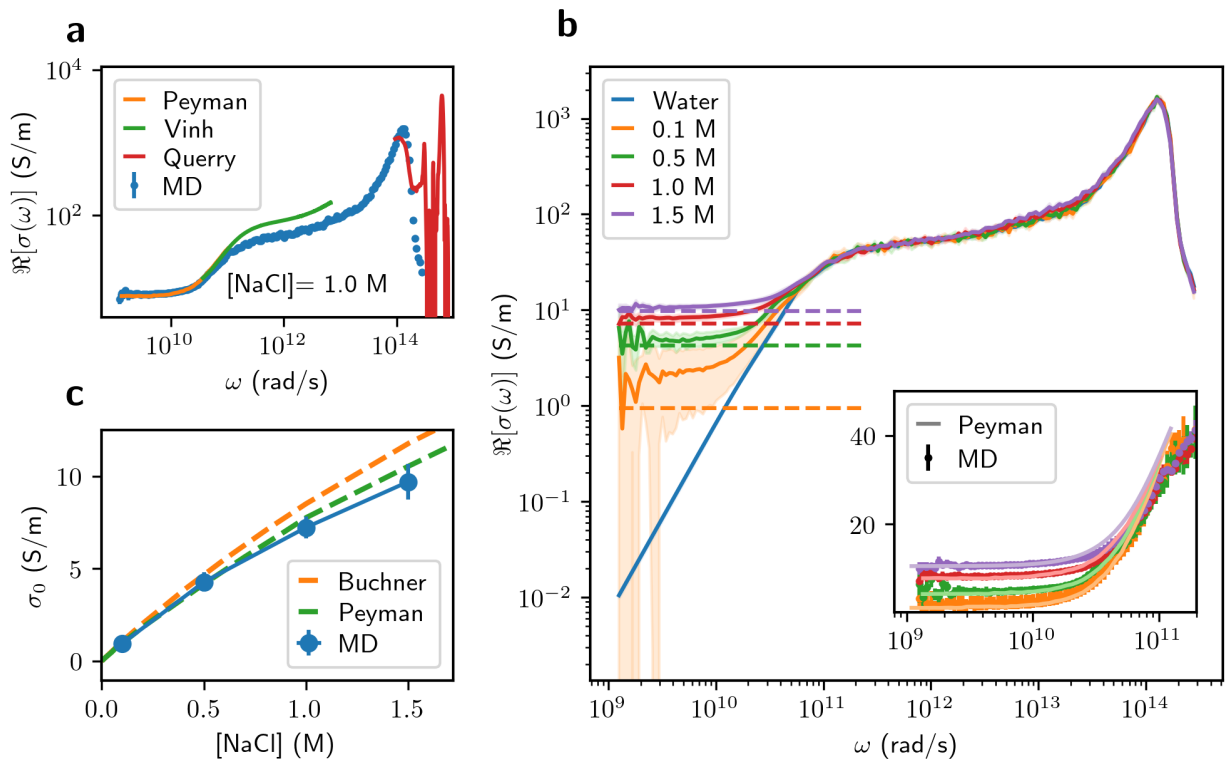

Figure 3: (a) Conductivity calculated from bulk simulations (symbols), as a function of frequency, for the 1 M system compared with experimental optical measurements (solid lines).[62–64] (b) Conductivity from bulk simulations for all the salt concentrations considered calculated using the GK (solid lines) and EH (dashed lines) approaches. The inset shows the low-frequency branches of conductivity from MD (symbols), compared with experimental measurements (solid lines) from Ref. 62. (c) Conductivity at zero frequency σ_0 from bulk simulations with the EH approach (symbols) and from experimental measurements[62,65] (dashed lines).

expect the global response to comprise "interfacial contributions" from electrolyte proximate to the electrodes, and a bulk-like contribution from the remaining electrolyte far from the electrodes. Experimentally, it can be challenging to rigorously disentangle such interfacial and bulk contributions to the charging dynamics.[66] Here, we exploit the fact that molecular simulations allow us to characterise the bulk response, by performing simulations of the electrolyte in the absence of any explicit interfaces (see *SI Appendix*). In particular, we use bulk simulations to estimate the electric conductivity σ in two distinct ways: (i) at finite frequencies $[\sigma(\omega)]$ using a Green-Kubo (GK) approach;[67] and (ii) at zero frequency $[\sigma_0 \equiv \sigma(0)]$ using the Einstein-Helfand (EH) approach.[68] [Note that, while $\sigma(\omega)$ is a complex

function, σ_0 is a real number.] More details on these calculations are provided in the *Methods* section.

Bulk electrolytes In Figure 3, we compare our bulk simulations with experimental results obtained with different spectroscopic techniques.[62–65] The experimental datasets were converted from permittivity to conductivity using the relation[67,69] $\sigma(\omega) = i\omega\varepsilon_0 [\varepsilon(\omega) - 1]$. The simulation results for the 1 M system reported in Fig. 3(a) show that $\Re[\sigma(\omega)]$ reaches a global maximum at $\omega \approx 1.5 \times 10^{14}$ rad/s corresponding to the water librational band.[70] At lower frequencies, we find a shoulder resembling the Debye-like modes of polar fluids and a plateau corresponding to σ_0. Comparing to experiments, we observe minor discrepancies; this is expected due to the limitations of the molecular model that we use. In particular, at high frequencies, the SPC/E model of water lacks any polarization modes resulting from intramolecular or electronic response.[70] Nonetheless, overall agreement across the whole frequency range is fair. In Fig. 3(b), we present $\Re[\sigma(\omega)]$ for all concentrations investigated. The dashed lines indicate σ_0 obtained by the EH method, which demonstrate the consistency between our two approaches to estimate the conductivity. (We note the large statistical errors for 0.1 M.) For concentrations other than 1 M, experimental data over the whole frequency range is scarcer, though we note that, similar to $Z(\omega)$, spectra overlap at high frequencies. Comparison to experimental data at low frequencies is shown in the inset, where we observe reasonable agreement with our simulation results. Figure 3(c) shows explicitly the comparison between σ_0 from simulation and $\Re[\sigma(\omega \to 0)]$ from experiment. While we find quantitative agreement at low concentrations, σ_0 is progressively underestimated at higher concentrations. Notwithstanding the limitations of the underlying model, the above analyses suggest that our bulk simulations faithfully capture the experimental conductivity of NaCl solutions.

Interfacial impedance and low-frequency behavior To discern the interfacial and bulk-like contributions to the impedance, we adopt a subtraction technique similar to that

used in experiments.[66] Specifically, we define the bulk-like impedance as that which describes a hypothetical system in which the electrolyte retains bulk-like characteristics over the whole volume that it occupies,

$$Z_{\mathrm{bulk}}(\omega) = \frac{d_{\mathrm{DDS}}}{A_{\mathrm{el}}} \frac{1}{\sigma(\omega)}. \tag{3}$$

The interfacial contribution $Z_{\mathrm{int}}(\omega)$ is then defined as the excess contribution to the total impedance:

$$Z_{\mathrm{int}}(\omega) = Z(\omega) - Z_{\mathrm{bulk}}(\omega). \tag{4}$$

We note that Z_{int} implicitly includes the two electrode-electrolyte interfaces; in our symmetric setup the contribution of a single interface is simply $Z_{\mathrm{int}}(\omega)/2$. The results for the real and imaginary parts of $Z_{\mathrm{int}}(\omega)$ are shown in Figs. 2(c) and (d), respectively.

For finite ion concentration, it is remarkable that $\Im[Z_{\mathrm{int}}(\omega \to 0)] \approx -1/\omega C_{\mathrm{diff}}$ is well-described by the static differential capacitance. This can be understood by acknowledging that, at low frequencies,

$$\Re[\sigma(\omega)] = \sigma_0 + \sigma_2 \omega^2 + \sigma_4 \omega^4 + \dots \tag{5}$$

$$\Im[\sigma(\omega)] = \sigma_1 \omega + \sigma_3 \omega^3 + \dots \tag{6}$$

where $\sigma_1 = \varepsilon_0(\varepsilon_{\mathrm{eff}} - 1)$, with $\varepsilon_{\mathrm{eff}}$ an effective, frequency-independent, dielectric constant of the solution.[69] As detailed in the *SI Appendix*, both the real and imaginary parts of the bulk conductivity are well described by these expansions (see Figs. S4 and S5), and it is straightforward to show that

$$\Im[Z_{\mathrm{int}}(\omega \to 0)] \approx -\frac{1}{\omega C_{\mathrm{diff}}} + \frac{\sigma_1 \omega}{\sigma_0^2 + (2\sigma_0\sigma_2 + \sigma_1^2)\omega^2} \frac{d_{\mathrm{DDS}}}{A_{\mathrm{el}}}. \tag{7}$$

Provided that $\sigma_0 > 0$, which is true for finite ion concentration, the second term (which describes $\Im[Z_{\mathrm{bulk}}(\omega)]$ well, see Fig. S7) vanishes as $\omega \to 0$. For dielectric systems such as pure water, however, this is no longer the case. As is apparent when setting $\sigma_0 = 0$ in

Eq. 7, we instead expect $\Im[Z_{\mathrm{w,int}}(\omega)] \sim -1/\omega C_{\mathrm{w,int}}$ with an effective interfacial differential capacitance

$$\frac{1}{C_{\mathrm{w,int}}} = \left[\frac{1}{C_{\mathrm{diff}}} - \frac{d_{\mathrm{DDS}}}{A_{\mathrm{el}}\varepsilon_0(\varepsilon_{\mathrm{w}}-1)}\right], \tag{8}$$

which, as seen in Fig. 2(d), describes the simulation data well. It clear from Eq. 8 that C_{diff} contains both interfacial and bulk contributions. For the $d = 5.07\,\mathrm{nm}$ system that we have investigated, we estimate that $C_{\mathrm{w,int}}/A_{\mathrm{el}} \approx 2.80\ \mu\mathrm{F/cm^2}$, while $\varepsilon_0(\varepsilon_{\mathrm{w}}-1)/d_{\mathrm{DDS}} \approx 13.17\ \mu\mathrm{F/cm^2}$. The total series capacitance $C_{\mathrm{diff}}/A_{\mathrm{el}} \approx 2.31\ \mu\mathrm{F/cm^2}$ is therefore dominated by the interfacial contribution. Evidently, as d_{DDS} increases, so too does the relative importance of the bulk contribution.

We now turn our attention to the real part of the interfacial impedance. Somewhat surprisingly, as shown in Fig. 2(c), we find that $\Re[Z_{\mathrm{int}}]$ is negligible to within statistical uncertainty; this is the case for all concentrations we investigate, including pure water. This suggests that the real part of the cell impedance $\Re[Z]$ behaves at low frequency as the bulk contribution (see *SI Appendix*:)

$$\Re[Z_{\mathrm{bulk}}(\omega \to 0)] \approx \frac{1}{\sigma_0}\left[1 - \left(\frac{\sigma_0\sigma_2 + \sigma_1^2}{\sigma_0^2}\right)\omega^2\right]\frac{d_{\mathrm{DDS}}}{A_{\mathrm{el}}}\,. \tag{9}$$

Fig. S6 shows that this expansion, using the parameters fitted on the conductivity $\sigma(\omega)$, describes well the bulk impedance at low frequency. For the confined case, a quadratic fit (see Fig. S8) allows to us to obtain the cell resistance $R = \Re[Z(\omega \to 0)]$. These different estimates for the resistance, together with those obtained using the EH and Nernst-Einstein values for σ_0, are summarized in Table S4. The inset of Fig. 2(c) confirms the good agreement between the corresponding confined $RA_{\mathrm{el}}/d_{\mathrm{DDS}}$ and bulk $\rho_{\mathrm{bulk}} = 1/\sigma_0$ resistivities, except for 0.1 M where $\rho \approx \rho_{\mathrm{bulk}}/3.6$. While it is possible that for this concentration the low-frequency regime might not be fully reached, we also note that the width of the EDL ($\lambda_D \approx 9.1$ Å) is only 5 times smaller than the interelectrode distance d and the separation between bulk and interfacial regions might be less straightforward (see also the discussion of timescales in

Section).

For pure water, σ_0 vanishes, and we obtain a qualitatively different behavior (see *SI Appendix*):

$$\Re[Z_{\mathrm{w,bulk}}(\omega \to 0)] \approx \frac{\sigma_2}{\sigma_1^2}\left[1 - \left(\frac{\sigma_2^2 + 2\sigma_1\sigma_3}{\sigma_1^2} - \frac{\sigma_4}{\sigma_2}\right)\omega^2\right]\frac{d_{\mathrm{DDS}}}{A_{\mathrm{el}}}, \tag{10}$$

with $\sigma_1 = \varepsilon_0(\varepsilon_{\mathrm{w}} - 1)$. In this case, the overall resistance of the cell is $R \approx R_{\mathrm{w,bulk}} = d_{\mathrm{DDS}}\sigma_2/[A_{\mathrm{el}}\varepsilon_0^2(\varepsilon_{\mathrm{w}}-1)^2]$. In the *SI Appendix*, we further show that within the Debye relaxation model, $\sigma_2 \approx \varepsilon_0(\varepsilon_{\mathrm{w}}-1)\tau_{\mathrm{w,bulk}}$, where $\tau_{\mathrm{w,bulk}} \approx 9\,\mathrm{ps}$ is the Debye relaxation time of bulk water. By fitting the bulk conductivity at low frequencies, we obtain an estimate $\sigma_2/\varepsilon_0(\varepsilon_{\mathrm{w}} - 1) \approx 10\,\mathrm{ps}$ consistent with this model.

Equivalent circuit model and effect of interelectrode distance From our analysis, we conclude that for finite salt concentrations the interfacial contribution to the impedance is mostly capacitive and is well-described by $Z_{\mathrm{int}}(\omega) \approx 1/i\omega C_{\mathrm{diff}}$. This is in stark contrast with recent findings on electrode-ionic liquid interfaces, where the resistance was dominated by interfacial contributions.[71] Our observations mean that we can model the total impedance of our systems as an equivalent circuit (EC) with a bulk component, parameterized on $\sigma(\omega)$ as in Eq. 3, in series with a purely capacitive element with $C_{\mathrm{diff}} = \beta\langle\delta Q^2\rangle$. Such EC models are already widely used by experimental groups to model macroscopic electrochemical cells with planar blocking electrodes.[66] It is worth emphasizing, however, that this work brings the first direct evidence of this behavior at the molecular scale and confirms the validity of these EC models to represent nanocapacitors.

Finally, we note that, to the extent that C_{diff} is independent of d, which we might reasonably expect if $\lambda_{\mathrm{D}} \ll d$ (see, e.g., Fig. S9), we can use this simple EC model to *predict* $Z(\omega)$ for different system sizes. We demonstrate this in Fig. 4, where we present results for $Z(\omega)$ for $2.5 \lesssim d/\mathrm{nm} \lesssim 20$. The results from simulation compare favorably to those predicted by $Z(\omega) = 1/i\omega C_{\mathrm{diff}} + d_{\mathrm{DDS}}/A_{\mathrm{el}}\sigma(\omega)$, where we have used C_{diff} obtained with $d = 5.07\,\mathrm{nm}$.

This suggests that, aside from the capacitive contribution arising from the EDL formation at the interface, the dielectric response of the confined electrolyte remains bulk-like. This observation is consistent with recent works that highlight how the dielectric response of nanoconfined water is essentially bulk-like, provided that one appropriately accounts for the boundary of the liquid.[16,54,72–75] Our results extend this conclusion to systems with dissolved ions.

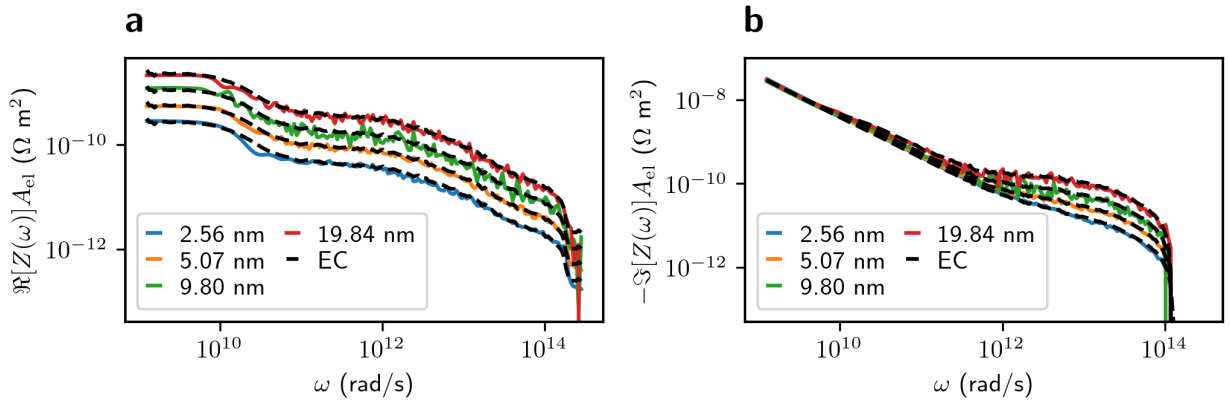

Figure 4: (a) Real and (b) imaginary parts of the impedance for different values of d (as indicated in the legends), for the 1 M electrolyte. The solid lines show results obtained from molecular simulations, while the dashed lines indicate the prediction of the simple EC model in which the interfacial impedance is purely capacitive. Importantly, the simple EC model has been parameterized with C_{diff} from a single simulation with $d = 5.07$ nm.

Effect of the salt concentration on relaxation times

As shown in previous work, for pure water confined between the gold-electrodes, the relaxation of the QACF is well-characterized by a single exponential with a characteristic time $\tau_{\text{w}} = \tau_{\text{w},\infty} d/[d + (\varepsilon_{\text{w}} - 1)w_{\text{DDS}}]$,[54] where $\tau_{\text{w},\infty} \approx 8.6$ ps is close to the bulk value for the Debye relaxation mode of water. Upon introducing ions, the QACF is broadly characterized by two timescales: a fast relaxation that is comparable to τ_{w}, and a much slower relaxation τ_{slow}, which depends on salt concentration [see Fig. 1(c)]. A global timescale can be defined

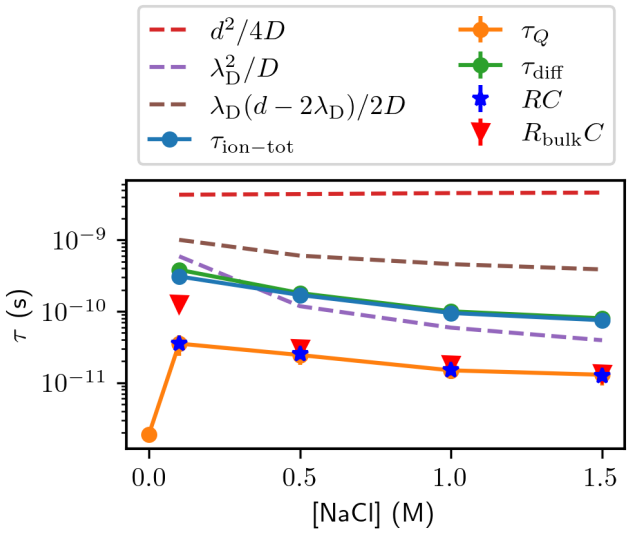

Figure 5: Comparison of relevant characteristic times as a function of salt concentration from simulations (symbols) and analytical theories (dashed lines).[31,33–35,76] τ_Q is calculated as the integral of the normalized QACFs (see Eq. 11). For $\tau_{ion-tot}$ (blue dots) and τ_{diff} (green dots), the characteristic time is extracted by fitting the data (see Figs. 6(b,c) and *SI Appendix*, Fig. S1) with exponential functions. The RC and $R_{bulk}C$ characteristic times use the resistance computed from confined and bulk simulations, respectively, and $C = C_{diff}$ from confined simulations. Note that R_{bulk} was calculated from the EH estimate of the bulk conductivity and using d_{DDS} instead of d, consistently with Eq. 3. Here, RC, $R_{bulk}C$, τ_Q and τ_{diff} were computed from equilibrium simulations, whereas $\tau_{ion-tot}$ was estimated from nonequilibrium simulations.

from the integral of the normalized QACF,[54]

$$\tau_Q = \int_0^\infty \frac{\langle \delta Q(0)\delta Q(t)\rangle}{\langle \delta Q^2\rangle}\,\mathrm{d}t, \tag{11}$$

such that the admittance behaves at low frequency as $Y(\omega) \approx i\omega C_{diff}/(1+i\omega\tau_Q)$. Consistent with our simple EC model, this translates in terms of impedance to $Z(\omega) \approx R + 1/i\omega C_{diff}$, with $R = \Re[Z(\omega \to 0)]$.

As shown in Fig. 5, beyond the initial jump from the pure water case (for which no ions from water autodissociation are captured by the present force field), τ_Q decreases with increasing ion concentration, but remains on the order 10^{-11} s. It is compared with the 'RC' times, using C_{diff} obtained from $\langle \delta Q^2\rangle$ [see Fig. 1(b)], and the total resistance estimated

either as $R_{\mathrm{bulk}} = d_{\mathrm{DDS}}/A_{\mathrm{el}}\sigma_0$ or $R = \Re[Z(\omega \to 0)]$ [see Fig. 2(a)]. As expected, RC_{diff} agrees well with τ_{Q} for the whole concentration range. The agreement obtained with R_{bulk} from bulk simulations is also good for the higher concentrations, but for the lowest concentration, 0.1 M, $R_{\mathrm{bulk}}C_{\mathrm{diff}}$ is approximately 3.6 times larger than τ_{Q}. As discussed above, this discrepancy between RC_{diff} and $R_{\mathrm{bulk}}C_{\mathrm{diff}}$ might be caused by the fact that we have not fully accessed the low frequency limit at 0.1 M, or simply due to the departure from the thin EDL limit ($\lambda_D \ll d$) where the interfacial and bulk contributions can be decoupled.

While the intermediate and high frequency range of $Z_{\mathrm{bulk}}(\omega)$ is dominated by the contribution of water, the behavior at low frequency significantly depends on the ions. We now examine three timescales frequently considered in the dynamics of ions in confined electrolytes obtained with analytical theories.[31,33–35,37,76] Such approaches are inherently approximate: they typically describe the solvent implicitly; use a common diffusion constant D for anions and cations; rely on mean-field assumptions; and use a simplified representation of the electrode-electrolyte interface. Therefore, we limit ourselves to examining qualitative trends with salt concentration rather than how well these time scales compare quantitatively with our simulations. The first timescale is $\tau_d = d^2/4D$, which corresponds to ion diffusion over the distance between the electrodes. The second timescale is the ionic Debye relaxation time $\tau_{\mathrm{D}} = \lambda_{\mathrm{D}}^2/D$, which corresponds to the relaxation of charge fluctuations in bulk electrolytes, with the diffusion of ions over the corresponding Debye screening length. The third timescale $\tau_{\mathrm{mix}} = \lambda_{\mathrm{D}}(d - 2\lambda_{\mathrm{D}})/2D$ mixes both λ_{D} and d;[31] it corresponds to the 'RC' charging time assuming Nernst-Einstein conductivity and DH capacitance and reduces to $\tau_{\mathrm{mix}} \approx \lambda_{\mathrm{D}}d/2D$ in the limit of thin EDLs. The time scales introduced so far can be broadly interpreted as approximations or limiting cases of the more general solution obtained within the Debye-Falkenhagen approximation by Janssen and Bier.[33]

We show these different time scales in Fig. 5 together with the simulation results for τ_{Q}. For the diffusion coefficient we use $D = 1.41 \times 10^{-9}$ m^2/s, the average diffusion coefficient of Na^+ and Cl^- ions computed from bulk simulations at 0.1 M. All the analytical timescales

overestimate the relaxation time, but with different orders of magnitudes and trends with salt concentration. The worst estimate is τ_d, by several orders of magnitude and no dependence on salt concentration; this result is not unsurprising as the build-up of EDLs does not require ions to diffuse over the whole electrochemical cell. While the order of magnitude of τ_{D} is correct for the highest concentrations we consider, the agreement with τ_Q is worse for the lower concentrations, with $\tau_{\mathrm{D}}/\tau_Q \approx 10$ at 0.1 M. Naively, we would expect such a mean-field prediction to *improve* as concentration is decreased. This discrepancy suggests the observation that $\tau_{\mathrm{D}} \sim \tau_Q$ for the higher concentrations is largely coincidental. Finally, despite the wrong order of magnitude, only τ_{mix} displays a trend with concentration similar to that of τ_{Q}. This observation suggests that τ_Q, and more generally the system's impedance, reflects the interplay between the dynamics of a bulk-like electrolyte and the interfacial capacitive behavior induced by the blocking electrodes. A more detailed discussion of the concentration dependence of τ_{D}, τ_{mix}, and τ_{Q} is included in the *SI Appendix* (see Fig. S10). In a bid to rationalize the quantitative disagreement between theory and simulation, in the next section, we probe the relaxation process in terms of contributions from ions, water and their cross correlations.

Water and ionic contributions

As shown in previous works, at $\Delta\Psi = 0$ V and with global electroneutrality, the total electrode charge Q is proportional to the total dipole moment of the solution M_{tot} in the direction perpendicular to the electrode surface.[54,77] For this reason, the behavior of $\langle \delta Q(0)\delta Q(t)\rangle$ is determined entirely by $\langle M_{\mathrm{tot}}(0)M_{\mathrm{tot}}(t)\rangle$. Clearly, in the case of an electrolyte solution, $M_{\mathrm{tot}}(t) = M_{\mathrm{wat}}(t) + M_{\mathrm{ion}}(t)$ has contributions from both the solvent water molecules and the dissolved ions. Molecular simulations offer the possibility of computing directly the ionic and solvent contributions, thus 'dissecting' the global response to understand the source of specific features, as shown in previous works.[78–80] We can therefore decompose the autocor-

relation function of the total dipole moment:

$$\langle \delta M_{\rm tot}(0)\delta M_{\rm tot}(t)\rangle = \langle \delta M_{\rm tot}(0)\delta M_{\rm ion}(t)\rangle + \langle \delta M_{\rm tot}(0)\delta M_{\rm wat}(t)\rangle, \tag{12}$$

with

$$\langle \delta M_{\rm tot}(0)\delta M_{\rm ion}(t)\rangle = \langle \delta M_{\rm ion}(0)\delta M_{\rm ion}(t)\rangle + \langle \delta M_{\rm wat}(0)\delta M_{\rm ion}(t)\rangle, \tag{13}$$

and

$$\langle \delta M_{\rm tot}(0)\delta M_{\rm wat}(t)\rangle = \langle \delta M_{\rm wat}(0)\delta M_{\rm wat}(t)\rangle + \langle \delta M_{\rm wat}(0)\delta M_{\rm ion}(t)\rangle. \tag{14}$$

The correlation functions on the right hand side of Eq. 12 rigorously relate the linear response of $M_{\rm ion}(t)$ and $M_{\rm wat}(t)$ to a change in voltage across the cell; consequently, they can be obtained by monitoring the time evolution of $M_{\rm ion}(t)$ and $M_{\rm wat}(t)$ upon the step change $\Delta\Psi = 0 \rightarrow 1$ V.

In Fig. 6(a), we present the static limit of these normalized decomposed dipole correlation functions. For all ion concentrations, the total comprises positive contributions from $\langle \delta M_{\rm ion}^2\rangle$ and $\langle \delta M_{\rm wat}^2\rangle$ and a large negative contribution from the cross correlation $\langle \delta M_{\rm ion}\delta M_{\rm wat}\rangle$. This anticorrelation between the equilibrium fluctuations of the ionic and solvent contributions to the polarization was also found in bulk systems,[78,79,81] and reflects the well-known Stillinger-Lovett (SL) conditions.[82,83] While Ref. 81 provided a framework to understand the SL conditions for the total dipole moment in bulk systems in terms of 'virtual electrodes' arising from the imposed boundary conditions, our results demonstrate that these SL conditions are also obeyed in the presence of explicit electrodes held at constant bias. See also Ref. 84.

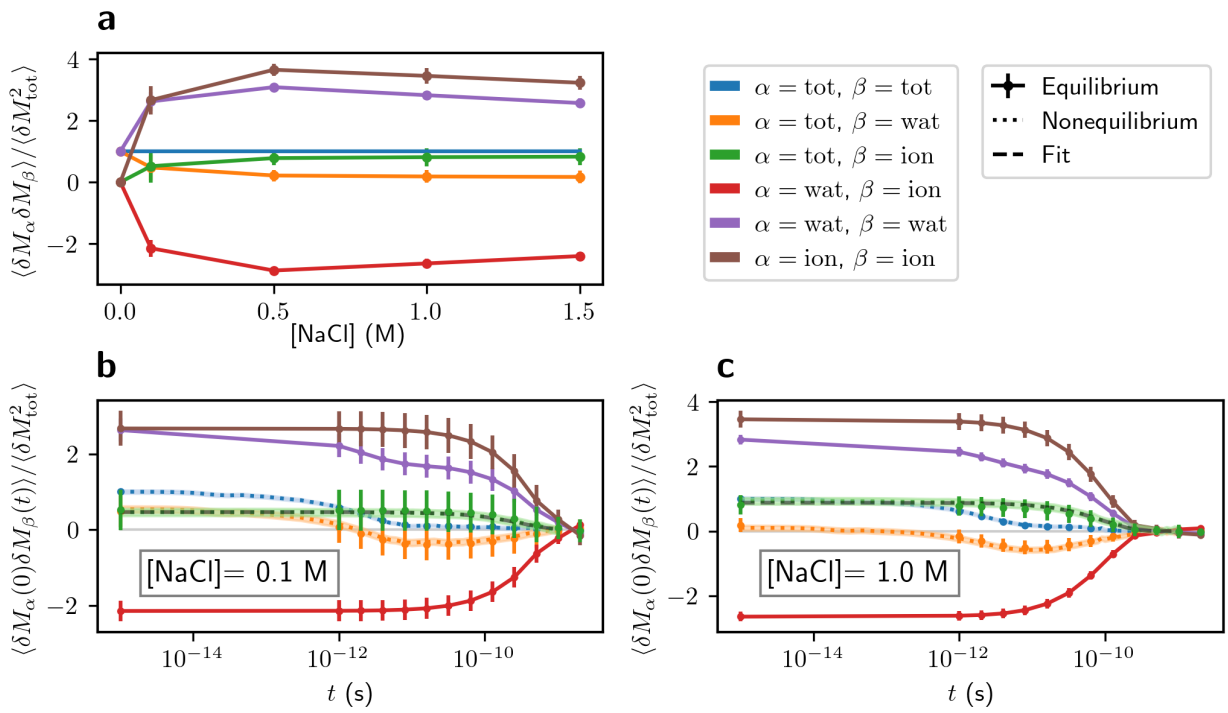

Figure 6: (a) Static correlations of the water and ionic contributions to the total dipole moment as a function salt concentration. (b,c) Normalized time correlation functions of the contributions to the total dipole moment for 0.1 M and 1.0 M salt concentrations, as a function of time. In all panels, each color indicates the same combination of contributions α and β. In panels (b,c), we compare the results of equilibrium simulations (lines with error bars), those of nonequilibrium simulations (dotted lines), and exponential fits (dashed lines).

We now turn our attention to the nonequilibrium relaxation of $M_{\rm ion}$ and $M_{\rm wat}$, shown in Fig. 6(b,c) for 0.1 M and 1.0 M, respectively. For both systems, we see an initial fast response of the solvent polarization (see dotted orange lines in Fig. 6(b,c)). In fact, the negative values of $\langle M_{\rm tot}(0) M_{\rm wat}(t) \rangle$ for $t \gtrsim 10^{-12}$ s indicate that the solvent polarization overshoots its equilibrium value (see Eq. S7 in the SI). On larger time scales, the ionic polarization begins to relax accompanied by further relaxation of the solvent polarization in an almost equal-and-opposite fashion. The relaxation of $M_{\rm ion}$ appears to follow a simple exponential time dependence, from which we can obtain an associated time scale $\tau_{\rm ion-tot}$. In Fig. 5 we plot $\tau_{\rm ion-tot}$ for all concentrations. Despite being roughly an order of magnitude smaller, we see that the dependence of $\tau_{\rm ion-tot}$ on concentration closely follows that of $\tau_{\rm mix}$. The observed anticorrelations between the solvent and ionic polarization during the system's

nonequilibrium response are reminiscent of the SL conditions at equilibrium, and consistent with recent observations in bulk electrolyte solutions at finite wavevector and frequency.[79] The impact of these anticorrelations appears to manifest as a much faster overall charging dynamics than predicted by ionic relaxation alone, as reflected by the order of magnitude discrepancy between $\tau_{\mathrm{ion-tot}}$ and τ_{Q}. Also shown in Fig. 6(b,c) are the correlation functions $\langle \delta M_{\mathrm{tot}}(0)\delta M_{\mathrm{ion}}(t)\rangle$ and $\langle \delta M_{\mathrm{tot}}(0)\delta M_{\mathrm{wat}}(t)\rangle$ obtained directly from the equilibrium fluctuations at $\Delta\Psi = 0\,\mathrm{V}$, albeit at a lower time resolution (full lines). As expected, these results agree with those obtained from our nonequilibrium simulations.

In an attempt to quantify the impact of introducing ions, we have computed $\langle \delta Q(0)\delta Q(t)\rangle_{\mathrm{diff}}$, by subtracting the pure water QACF from the QACF at finite salt concentration. We find that, for all investigated concentrations, $\langle \delta Q(0)\delta Q(t)\rangle_{\mathrm{diff}}$ is well-described by a simple exponential with characteristic time τ_{diff} (see Fig. S1). The behavior of τ_{diff} with concentration is shown in Fig. 5. For all concentrations, τ_{diff} is roughly seven times larger than τ_Q and comparable to $\tau_{\mathrm{ion-tot}}$. While it is tempting to attribute fast and slow timescales in the system into motions that involve ions and those that do not, such a decomposition is not straightforward. This can be seen in Fig. 6(b,c), where we further decompose the equilibrium correlation functions according to Eqs. 13 and 14. Not only do we see that $\langle \delta M_{\mathrm{ion}}(0)\delta M_{\mathrm{ion}}(t)\rangle$ and $\langle \delta M_{\mathrm{ion}}(0)\delta M_{\mathrm{wat}}(t)\rangle$ decay slowly, but so too does $\langle \delta M_{\mathrm{wat}}(0)\delta M_{\mathrm{wat}}(t)\rangle$. In other words, fast and slow relaxation cannot be separated into purely solvent and ionic contributions.

To summarize, we find that analytical theories and implicit solvent descriptions can describe the qualitative scaling of the relaxation time scales with concentration. However, these predictions are far from quantitative agreement with simulation results. Our MD results highlight: (i) ion and water polarization are strongly anticorrelated, and this effect is persistent in time; and (ii) ion and water polarization relax with different time scales (single exponential with $\tau_{\mathrm{ion-tot}}$, and a combination of τ_{w} and $\tau_{\mathrm{ion-tot}}$, respectively). These two features are absent in most analytical theories of electrolytes and present a significant challenge for implicit solvent models to faithfully capture relaxation in EDL capacitors.

Conclusions

In this work, we employed molecular dynamics simulations to study electrode charge and polarization dynamics in gold/NaCl(aq) nanocapacitors. Using both equilibrium and nonequilibrium simulations, we investigated the impact of ion concentration and interelectrode distance on the charging dynamics. As expected, we found that ions induce slower dynamics compared to pure water systems, and more concentrated solutions result in faster charge relaxation. Using equilibrium charge autocorrelation functions, we obtained impedance spectra for the nanocapacitors that exhibit features typical for systems with blocking electrodes. Exploiting the fact that we can obtain the bulk conductivity directly in molecular simulations, we showed that the total impedance is well-described by a simple sum of interfacial and bulk contributions. Remarkably, we found that the interfacial impedance for the considered systems is purely capacitive, *i.e.*, interfacial resistance is negligible. We demonstrated that this simple EC model permits extrapolation to larger system sizes; while nanocapacitors are interesting in their own right, this observation will help to bridge the gap between molecular simulations and EIS experiments on larger length scales. We also showed that the electrolyte response, aside from the capacitive interfacial contribution, remains bulk-like even when the interelectrode separation is only a few nanometers.

Future work could focus on the influence of more complicated, possibly porous[42,58] and heterogeneous electrode-electrolyte interfaces,[85] as well as on the effect of screening within the electrode material via the Thomas-Fermi length,[86,87] many-body interactions at the surface (as done *e.g.* for water on platinum electrodes[88,89]) or even non-adiabatic effects.[12] The same methodology could be applied and we expect the main conclusions to hold for a variety of non-reactive systems. If these more elaborate descriptions of the electrode material induce specific ion binding to the surface, this may require longer simulations to correctly sample the adsorption/desorption processes, but would in turn provide a direct link between the measured frequency-dependent impedance and the corresponding processes (possibly via more complex EC models, as often done to analyze experiments). Furthermore, the present

theoretical framework to predict and analyze the impedance could be extended to include interfacial electron-transfer phenomena at a classical level,[90] which would allow representing devices such as pseudocapacitors and batteries.

We also investigated the most relevant characteristic times of charge and polarization relaxation. While we found that analytical predictions fail to quantitatively describe the simulation results, they succeed in reproducing the qualitative behavior. By dissecting the global response into contributions from the ionic and solvent polarization, we showed that the failure of the analytic predictions originates from an anti-correlation between ions and water. In particular, we found that not only do the ions themselves relax slowly, but their presence also introduces a slow time scale in the solvent relaxation. Future coarse-grained descriptions of confined electrolytes could include the nonlocality and frequency-dependence of the solvent response[79,91] beyond a uniform static permittivity[36,92] to restore, at least partially, this fundamental physics.

Methods

Numerical simulations

Classical molecular dynamics simulations were performed using MetalWalls[93,94] and LAMMPS[95] (equipped with the ELECTRODE package[96]), which allows for the computation of custom properties on-the-fly. Equivalent simulations performed on the two software packages yielded consistent results, as already checked by other authors on similar systems.[96] In this work, we simulated two different kinds of systems: bulk and confined simulations. The force field pameterization and simulation setups are similar to those used in previous works.[86] Bulk simulations of the electrolyte, described by a simple point charge model (i.e., water with the SPC/E model[97] and NaCl ions modelled as Lennard-Jones particles with point charges[98]), were performed with 3D periodic boundary conditions (PBCs) with "tin-foil" boundary conditions. The confined system also included gold electrodes modelled as Lennard-Jones

particles[99] with a gaussian charge density fluctuating in magnitude (see below). Simulations performed with MetalWalls were carried out under 2D PBCs, while those with LAMMPS used 3D PBCs and a finite field to impose $\Delta\Psi$.[100,101] In all the confined simulations, the spacing between the electrodes d was equilibrated at constant atmospheric pressure and production runs were carried out at fixed separation. All the simulations are performed in the NVT ensemble and the temperature is fixed at 298 K using a Nosé–Hoover chain thermostat,[102] with 5 chained thermostats having all the same time constant of 1 ps. In confined simulations, we enforce the additional constraints of constant applied potential and global electroneutrality. The constant potential condition is ensured by the fluctuating charge method.[38]

More simulation details and a list of all simulation runs can be found in the *SI Appendix*.

Frequency-dependent impedance from charge fluctuations and bulk conductivity spectrum

The frequency-dependent electrical impedance and admittance were calculated from the dynamics of the equilibrium fluctuations of the electrode charge sampled from MD simulations, using the fluctuation-dissipation relation introduced in our previous work:[54]

$$Y(\omega) = \beta \left[i\omega \langle \delta Q^2 \rangle + \omega^2 \int_0^\infty \langle \delta Q(0) \delta Q(t) \rangle e^{-i\omega t} \mathrm{d}t \right], \tag{15}$$

where $Y = 1/Z$ is the admittance, Z is the impedance, $\beta = 1/k_\mathrm{B}T$ with k_B the Boltzmann constant and T the temperature, ω is the angular frequency, Q is the electrode charge, and $\delta Q = Q - \langle Q \rangle$, with $\langle \cdot \rangle$ denoting the canonical average. The numerical calculation of the Fourier-Laplace transform in Eq. 15 was performed as in Ref. 54, using Filon-Lagrange integration and by applying a windowing procedure to $\langle \delta Q(0) \delta Q(t) \rangle$ to suppress the numerical noise at large times. In this work, we used a normalized version of the windowing function, which allows preserving the magnitude of the original function at short times. A direct

comparison between the raw and windowed autocorrelation functions is shown in the *SI Appendix*, Figs. S10, S11 and S12.

In principle, the frequency-dependent conductivity in bulk systems can be estimated from the dynamics of the total dipole moment $\mathbf{M}$, calculated with unwrapped coordinates and including both salt and solvent species.[67] In particular, the susceptibility $\chi(\omega)$ can be estimated from the total dipole moment[69] via

$$\chi(\omega) = \frac{\beta}{3V}\left[\langle \delta\mathbf{M}^2\rangle - i\omega\int_0^\infty \langle \delta\mathbf{M}(0)\delta\mathbf{M}(t)\rangle e^{-i\omega t}\mathrm{d}t\right], \tag{16}$$

where V is the system volume. The frequency-dependent conductivity can be then calculated as

$$\sigma(\omega) = i\omega\chi(\omega) = i\omega\chi'(\omega) - \omega\chi''(\omega), \tag{17}$$

where χ' and χ'' denote the real and imaginary parts of the susceptibility. We used this approach to estimate the frequency-dependent conductivity from bulk water simulations. In the presence of free charge carriers (i.e., for finite salt concentrations), $\langle \mathbf{M}^2\rangle$ becomes a divergent quantity, so the frequency-dependent conductivity has to be calculated using a different approach. The problem can be circumvented using electric currents $\mathbf{J}(t) = d\mathbf{M}/dt$ instead of the total polarization.[67] The conductivity can be rewritten in the following form

$$\sigma(\omega) = \frac{\beta}{3V}\int_0^\infty \langle \delta\mathbf{J}(0)\delta\mathbf{J}(t)\rangle e^{-i\omega t}\mathrm{d}t. \tag{18}$$

The Fourier-Laplace transform in Eqs. 16 and 18 was calculated numerically with the same windowing and integration scheme used to solve the transform in Eq. 15.

For finite salt concentrations, the DC conductivity $[\sigma(\omega \to 0) = \sigma_0]$ can be estimated from the behavior of $\Re[\sigma(\omega)]$ at low frequency (see Fig. S5 in the *SI Appendix).* Alternatively, it can be computed using the Einstein-Helfand formalism which relates the total dipole moment

of ions $\mathbf{M}_{\text{ion}}$ to σ_0:[68]

$$\lim_{t\to\infty}\langle\Delta\mathbf{M}_{\text{ion}}^2(t)\rangle = \frac{6V}{\beta}\sigma_0 t + 2\langle\mathbf{M}_{\text{ion}}^2\rangle, \tag{19}$$

where t is the time. In practice, we fit $\langle\Delta\mathbf{M}_{\text{ion}}^2(t)\rangle$ with a line and extract σ_0 from the slope of the fitted line (see Fig. S2 in the *SI Appendix*).

Data availability

Input files and raw data for figures have been deposited on Zenodo.[103]

Acknowledgements

The authors acknowledge fruitful discussions with Mathieu Salanne, Michiel Sprik, Clare Grey and Mathijs Janssen. S.J.C. is a Royal Society University Research Fellow (Grant No. URF\R1\211144) at the University of Cambridge. SPN acknowledges funding from the European Union's Horizon 2020 Research and Innovation Program under Grant Agreement No. 957189 (BIG-MAP project). G. P. and B. R. acknowledge funding from the European Research Council under the European Union's Horizon 2020 research and innovation program (project SENSES, grant Agreement No. 863473). G. P. and B. R. acknowledge access to HPC resources from GENCI-IDRIS (grant no. 2022-AD010912966R1).

References

1. Robin, P.; Kavokine, N.; Bocquet, L. Modeling of emergent memory and voltage spiking in ionic transport through angstrom-scale slits. *Science* **2021**, *373*, 687–691.

2. Chun, H.; Chung, T. D. Iontronics. *Annual Review of Analytical Chemistry* **2015**, *8*, 441–462.

3. Singh, P. S.; Kätelhön, E.; Mathwig, K.; Wolfrum, B.; Lemay, S. G. Stochasticity in Single-Molecule Nanoelectrochemistry: Origins, Consequences, and Solutions. *ACS Nano* **2012**, *6*, 9662–9671.

4. Lemay, S. G.; Kang, S.; Mathwig, K.; Singh, P. S. Single-Molecule Electrochemistry: Present Status and Outlook. *Accounts of Chemical Research* **2013**, *46*, 369–377.

5. Keyser, U. F.; Koeleman, B. N.; Van Dorp, S.; Krapf, D.; Smeets, R. M. M.; Lemay, S. G.; Dekker, N. H.; Dekker, C. Direct force measurements on DNA in a solid-state nanopore. *Nature Physics* **2006**, *2*, 473–477.

6. Pech, D.; Brunet, M.; Durou, H.; Huang, P.; Mochalin, V.; Gogotsi, Y.; Taberna, P.-L.; Simon, P. Ultrahigh-power micrometre-sized supercapacitors based on onion-like carbon. *Nature Nanotechnology* **2010**, *5*, 651–654.

7. Marbach, S.; Bocquet, L. Osmosis, from molecular insights to large-scale applications. *Chemical Society Reviews* **2019**, *48*, 3102–3144.

8. Hatsuki, R.; Yujiro, F.; Yamamoto, T. Direct measurement of electric double layer in a nanochannel by electrical impedance spectroscopy. *Microfluidics and Nanofluidics* **2013**, *14*, 983–988.

9. Sun, P.; Mirkin, M. V. Electrochemistry of Individual Molecules in Zeptoliter Volumes. *Journal of the American Chemical Society* **2008**, *130*, 8241–8250.

10. Secchi, E.; Marbach, S.; Niguès, A.; Stein, D.; Siria, A.; Bocquet, L. Massive radius-dependent flow slippage in carbon nanotubes. *Nature* **2016**, *537*, 210–213.

11. Kavokine, N.; Bocquet, M.-L.; Bocquet, L. Fluctuation-induced quantum friction in nanoscale water flows. *Nature* **2022**, *602*, 84–90.

12. Bui, A. T.; Thiemann, F. L.; Michaelides, A.; Cox, S. J. Classical Quantum Friction at Water–Carbon Interfaces. *Nano Letters* **2023**, *23*, 580–587.

13. Fumagalli, L.; Esfandiar, A.; Fabregas, R.; Hu, S.; Ares, P.; Janardanan, A.; Yang, Q.; Radha, B.; Taniguchi, T.; Watanabe, K.; Gomila, G.; Novoselov, K. S.; Geim, A. K. Anomalously low dielectric constant of confined water. *Science* **2018**, *360*, 1339–1342.

14. Motevaselian, M. H.; Aluru, N. R. Universal Reduction in Dielectric Response of Confined Fluids. *ACS Nano* **2020**, *14*, 12761–12770.

15. Olivieri, J.-F.; Hynes, J. T.; Laage, D. Confined Water's Dielectric Constant Reduction Is Due to the Surrounding Low Dielectric Media and Not to Interfacial Molecular Ordering. *The Journal of Physical Chemistry Letters* **2021**, *12*, 4319–4326, Publisher: American Chemical Society.

16. Bonthuis, D. J.; Gekle, S.; Netz, R. R. Dielectric profile of interfacial water and its effect on double-layer capacitance. *Physical Review Letters* **2011**, *107*, 166102.

17. Underwood, T. R.; Bourg, I. C. Dielectric Properties of Water in Charged Nanopores. *The Journal of Physical Chemistry B* **2022**, *126*, 2688–2698.

18. Borgis, D.; Laage, D.; Belloni, L.; Jeanmairet, G. Dielectric response of confined water films from a classical density functional theory perspective. *Chemical Science* **2023**, 10.1039.D3SC01267K.

19. Jiménez-Ángeles, F.; Harmon, K. J.; Nguyen, T. D.; Fenter, P.; Olvera de la Cruz, M. Nonreciprocal interactions induced by water in confinement. *Physical Review Research* **2020**, *2*, 043244.

20. Mei, B.-A.; Munteshari, O.; Lau, J.; Dunn, B.; Pilon, L. Physical Interpretations of Nyquist Plots for EDLC Electrodes and Devices. *The Journal of Physical Chemistry C* **2018**, *122*, 194–206.

21. Wang, S.; Zhang, J.; Gharbi, O.; Vivier, V.; Gao, M.; Orazem, M. E. Electrochemical impedance spectroscopy. *Nature Reviews Methods Primers* **2021**, *1*, 41.

22. Segalini, J.; Daffos, B.; Taberna, P.; Gogotsi, Y.; Simon, P. Qualitative Electrochemical Impedance Spectroscopy study of ion transport into sub-nanometer carbon pores in Electrochemical Double Layer Capacitor electrodes. *Electrochimica Acta* **2010**, *55*, 7489–7494.

23. Taberna, P.-L.; Simon, P.; Fauvarque, J.-F. Electrochemical Characteristics and Impedance Spectroscopy Studies of Carbon-Carbon Supercapacitors. *J. Electrochem. Soc.* **2003**, *150*, A292–A300.

24. Vivier, V.; Orazem, M. E. Impedance Analysis of Electrochemical Systems. *Chemical Reviews* **2022**, *122*, 11131–11168, Publisher: American Chemical Society.

25. Dion, F.; Lasia, A. The use of regularization methods in the deconvolution of underlying distributions in electrochemical processes. *Journal of Electroanalytical Chemistry* **1999**, *475*, 28–37.

26. Biesheuvel, P. M.; Bazant, M. Z. Nonlinear Dynamics of Capacitive Charging and Desalination by Porous Electrodes. *Phys. Rev. E* **2010**, *81*, 031502.

27. Lian, C.; Janssen, M.; Liu, H.; van Roij, R. Blessing and Curse: How a Supercapacitor's Large Capacitance Causes its Slow Charging. *Phys. Rev. Lett.* **2020**, *124*, 076001.

28. Lin, Y.; Lian, C.; Berrueta, M. U.; Liu, H.; van Roij, R. Microscopic Model for Cyclic Voltammetry of Porous Electrodes. *Physical Review Letters* **2022**, *128*, 206001, Publisher: American Physical Society.

29. Pedersen, C.; Aslyamov, T.; Janssen, M. Equivalent Circuit and Continuum Modeling of the Impedance of Electrolyte-Filled Pores. *PRX Energy* **2023**, *2*, 043006.

30. Lasia, A. The Origin of the Constant Phase Element. *The Journal of Physical Chemistry Letters* **2022**, *13*, 580–589.

31. Bazant, M. Z.; Thornton, K.; Ajdari, A. Diffuse-charge dynamics in electrochemical systems. *Phys. Rev. E* **2004**, *70*, 021506.

32. Barbero, G.; Alexe-Ionescu, A. L. Role of the diffuse layer of the ionic charge on the impedance spectroscopy of a cell of liquid. *Liquid Crystals* **2005**, *32*, 943–949.

33. Janssen, M.; Bier, M. Transient Dynamics of Electric Double-Layer Capacitors: Exact Expressions Within the Debye-Falkenhagen Approximation. *Phys. Rev. E* **2018**, *97*, 052616.

34. Palaia, I.; Asta, A. J.; Warren, P. B.; Rotenberg, B.; Trizac, E. Poisson-Nernst-Planck charging dynamics of an electric double layer capacitor: symmetric and asymmetric binary electrolytes. *arXiv* **2023**, arxiv:2303.07859 [cond-mat.soft].

35. Palaia, I.; Asta, A. J.; Warren, P. B.; Rotenberg, B.; Trizac, E. Charging dynamics of electric double layer nanocapacitors in mean-field. *arXiv* **2023**, arxiv:2301.00610 [physics.chem-ph].

36. Cats, P.; Sitlapersad, R. S.; den Otter, W. K.; Thornton, A. R.; van Roij, R. Capacitance and Structure of Electric Double Layers: Comparing Brownian Dynamics and Classical Density Functional Theory. *Journal of Solution Chemistry* **2021**,

37. Asta, A. J.; Palaia, I.; Trizac, E.; Levesque, M.; Rotenberg, B. Lattice Boltzmann electrokinetics simulation of nanocapacitors. *J. Chem. Phys.* **2019**, *151*, 114104.

38. Scalfi, L.; Salanne, M.; Rotenberg, B. Molecular Simulation of Electrode-Solution Interfaces. *Annual Review of Physical Chemistry* **2021**, *72*, 189.

39. Jeanmairet, G.; Rotenberg, B.; Salanne, M. Microscopic Simulations of Electrochemical Double-Layer Capacitors. *Chemical Reviews* **2022**, *122*, 10860–10898, PMID: 35389636.

40. Alfarano, S. R.; Pezzotti, S.; Stein, C. J.; Lin, Z.; Sebastiani, F.; Funke, S.; Hoberg, C.; Kolling, I.; Ma, C. Y.; Mauelshagen, K.; Ockelmann, T.; Schwaab, G.; Fu, L.;

Brubach, J.-B.; Roy, P.; Head-Gordon, M.; Tschulik, K.; Gaigeot, M.-P.; Havenith, M. Stripping away ion hydration shells in electrical double-layer formation: Water networks matter. *Proceedings of the National Academy of Sciences* **2021**, *118*, e2108568118.

41. Son, C. Y.; Wang, Z.-G. Image-charge effects on ion adsorption near aqueous interfaces. *Proceedings of the National Academy of Sciences* **2021**, *118*, e2020615118.

42. Merlet, C.; Rotenberg, B.; Madden, P. A.; Taberna, P.-L.; Simon, P.; Gogotsi, Y.; Salanne, M. On the Molecular Origin of Supercapacitance in Nanoporous Carbon Electrodes. *Nat. Mater.* **2012**, *11*, 306–310.

43. Péan, C.; Merlet, C.; Rotenberg, B.; Madden, P. A.; Taberna, P.-L.; Daffos, B.; Salanne, M.; Simon, P. On the dynamics of charging in nanoporous carbon-based supercapacitors. *ACS Nano* **2014**, *8*, 1576–1583.

44. Péan, C.; Rotenberg, B.; Simon, P.; Salanne, M. Multi-scale Modelling of Supercapacitors: From molecular Simulations to a Transmission Line Model. *J. Power Sources* **2016**, *326*, 680–685.

45. Bi, S.; Salanne, M. Co-Ion Desorption as the Main Charging Mechanism in Metallic 1T-MoS_2 Supercapacitors. *ACS Nano* **2022**, *16*, 18658–18666.

46. Siepmann, J. I.; Sprik, M. Influence of Surface-Topology and Electrostatic Potential on Water Electrode Systems. *J. Chem. Phys.* **1995**, *102*, 511–524.

47. Reed, S. K.; Lanning, O. J.; Madden, P. A. Electrochemical interface between an ionic liquid and a model metallic electrode. *J. Chem. Phys.* **2007**, *126*, 084704, Publisher: American Institute of Physics.

48. Scalfi, L.; Limmer, D. T.; Coretti, A.; Bonella, S.; Madden, P. A.; Salanne, M.; Rotenberg, B. Charge fluctuations from molecular simulations in the constant-potential ensemble. *Phys. Chem. Chem. Phys.* **2020**, *22*, 10480–10489.

49. Nyquist, H. Thermal Agitation of Electric Charge in Conductors. *Phys. Rev.* **1928**, *32*, 110.

50. Johnson, J. Thermal Agitation of Electricity in Conductors. *Phys. Rev.* **1928**, *32*, 97.

51. De Haas-Lorentz, G. L. Over De Theorie Van De Brown'sche Beweging En Daarmede Verwante Verschijnselen. Ph.D. thesis, Rijks-Universiteit Te Leiden,, 1912.

52. Limmer, D. T.; Merlet, C.; Salanne, M.; Chandler, D.; Madden, P. A.; van Roij, R.; Rotenberg, B. Charge Fluctuations in Nanoscale Capacitors. *Phys. Rev. Lett.* **2013**, *111*.

53. Uralcan, B.; Aksay, I. A.; Debenedetti, P. G.; Limmer, D. T. Concentration Fluctuations and Capacitive Response in Dense Ionic Solutions. *J. Phys. Chem. Letters* **2016**, *7*, 2333–2338.

54. Pireddu, G.; Rotenberg, B. Frequency-Dependent Impedance of Nanocapacitors from Electrode Charge Fluctuations as a Probe of Electrolyte Dynamics. *Phys. Rev. Lett.* **2023**, *130*, 098001.

55. Serva, A.; Scalfi, L.; Rotenberg, B.; Salanne, M. Effect of the metallicity on the capacitance of gold–aqueous sodium chloride interfaces. *The Journal of Chemical Physics* **2021**, *155*, 044703, Publisher: American Institute of Physics.

56. Park, S.; McDaniel, J. G. Helmholtz Capacitance of Aqueous NaCl Solutions at the Au(100) Electrode from Polarizable and Nonpolarizable Molecular Dynamics Simulations. *The Journal of Physical Chemistry C* **2022**, *126*, 16461–16476.

57. Ntim, S.; Sulpizi, M. Molecular dynamics simulations of electrified interfaces including the metal polarisation. *Physical Chemistry Chemical Physics* **2023**, *25*, 22619–22625.

58. Simoncelli, M.; Ganfoud, N.; Sene, A.; Haefele, M.; Daffos, B.; Taberna, P.-L.; Salanne, M.; Simon, P.; Rotenberg, B. Blue Energy and Desalination with Nanoporous

Carbon Electrodes: Capacitance from Molecular Simulations to Continuous Models. *Physical Review X* **2018**, *8*, 021024.

59. Khademi, M.; Barz, D. P. J. Structure of the Electrical Double Layer Revisited: Electrode Capacitance in Aqueous Solutions. *Langmuir* **2020**, *36*, 4250–4260.

60. Rami Reddy, M.; Berkowitz, M. The dielectric constant of SPC/E water. *Chemical Physics Letters* **1989**, *155*, 173–176.

61. Rotenberg, B.; Bernard, O.; Hansen, J.-P. Underscreening in ionic liquids: a first principles analysis. *Journal of Physics: Condensed Matter* **2018**, *30*, 054005.

62. Peyman, A.; Gabriel, C.; Grant, E. Complex permittivity of sodium chloride solutions at microwave frequencies. *Bioelectromagnetics* **2007**, *28*, 264–274.

63. Vinh, N. Q.; Sherwin, M. S.; Allen, S. J.; George, D. K.; Rahmani, A. J.; Plaxco, K. W. High-precision gigahertz-to-terahertz spectroscopy of aqueous salt solutions as a probe of the femtosecond-to-picosecond dynamics of liquid water. *The Journal of Chemical Physics* **2015**, *142*, 164502.

64. Querry, M. R.; Waring, R. C.; Holland, W. E.; Hale, G. M.; Nijm, W. Optical Constants in the Infrared for Aqueous Solutions of NaClt. *Journal of the Optical Society of America* **1972**, *62*.

65. Buchner, R.; Hefter, G. T.; May, P. M. Dielectric Relaxation of Aqueous NaCl Solutions. *The Journal of Physical Chemistry A* **1999**, *103*, 1–9.

66. Chassagne, C.; Dubois, E.; Jiménez, M. L.; Van Der Ploeg, J. P. M.; Van Turnhout, J. Compensating for Electrode Polarization in Dielectric Spectroscopy Studies of Colloidal Suspensions: Theoretical Assessment of Existing Methods. *Frontiers in Chemistry* **2016**, *4*.

67. Sega, M.; Kantorovich, S. S.; Arnold, A.; Holm, C. In *Recent Advances in Broadband Dielectric Spectroscopy*; Kalmykov, Y. P., Ed.; Springer Netherlands: Dordrecht, 2013; pp 103–122, Series Title: NATO Science for Peace and Security Series B: Physics and Biophysics.

68. Schröder, C.; Haberler, M.; Steinhauser, O. On the computation and contribution of conductivity in molecular ionic liquids. *J. Chem. Phys.* **2008**, *128*, 134501.

69. Hansen, J.-P.; McDonald, I. *Theory of simple liquids*, 4th ed.; Academic Press, 1986.

70. Carlson, S.; Brünig, F. N.; Loche, P.; Bonthuis, D. J.; Netz, R. R. Exploring the Absorption Spectrum of Simulated Water from MHz to Infrared. *The Journal of Physical Chemistry A* **2020**, *124*, 5599–5605.

71. Dufils, T.; Sprik, M.; Salanne, M. Computational Amperometry of Nanoscale Capacitors in Molecular Simulations. *The Journal of Physical Chemistry Letters* **2021**, *12*, 4357–4361, Publisher: American Chemical Society.

72. Cox, S. J.; Geissler, P. L. Dielectric response of thin water films: a thermodynamic perspective. *Chem. Sci.* **2022**, *13*, 9102–9111.

73. Cox, S. J. Dielectric response with short-ranged electrostatics. *Proceedings of the National Academy of Sciences* **2020**, *117*, 19746–19752.

74. Zhang, C. Note: On the dielectric constant of nanoconfined water. *The Journal of Chemical Physics* **2018**, *148*, 156101.

75. Coquinot, B.; Becker, M.; Netz, R.; Bocquet, L.; Kavokine, N. Collective modes and quantum effects in two-dimensional nanofluidic channels. *Faraday Discussions* **2023**, Advance Article.

76. Hoang Ngoc Minh, T.; Stoltz, G.; Rotenberg, B. Frequency and field-dependent response of confined electrolytes from Brownian dynamics simulations. *The Journal of Chemical Physics* **2023**, *158*, 104103.

77. Takae, K.; Onuki, A. Fluctuations of local electric field and dipole moments in water between metal walls. *J. Chem. Phys.* **2015**, *143*, 154503.

78. Rinne, K. F.; Gekle, S.; Netz, R. R. Dissecting ion-specific dielectric spectra of sodium-halide solutions into solvation water and ionic contributions. *The Journal of Chemical Physics* **2014**, *141*, 214502.

79. Hoang Ngoc Minh, T.; Kim, J.; Pireddu, G.; Chubak, I.; Nair, S.; Rotenberg, B. Electrical noise in electrolytes: a theoretical perspective. *Faraday Discuss.* **2023**, *246*, 198.

80. Carof, A.; Marry, V.; Salanne, M.; Hansen, J.-P.; Turq, P.; Rotenberg, B. Coarse graining the dynamics of nano-confined solutes: the case of ions in clays. *Molecular Simulation* **2014**, *40*, 237–244.

81. Cox, S. J.; Sprik, M. Finite field formalism for bulk electrolyte solutions. *The Journal of Chemical Physics* **2019**, *151*, 064506, Publisher: AIP Publishing LLCAIP Publishing.

82. Stillinger, F. H.; Lovett, R. General Restriction on the Distribution of Ions in Electrolytes. *The Journal of Chemical Physics* **1968**, *49*, 1991–1994, Publisher: American Institute of Physics.

83. Stillinger, F. H.; Lovett, R. Ion-Pair Theory of Concentrated Electrolytes. I. Basic Concepts. *The Journal of Chemical Physics* **1968**, *48*, 3858–3868, Publisher: American Institute of Physics.

84. Carnie, S. L. On sum rules and Stillinger–Lovett conditions for inhomogeneous Coulomb systems. *J. Chem. Phys.* **1983**, *78*, 2742–2745.

85. Dufils, T.; Knijff, L.; Shao, Y.; Zhang, C. PiNNwall: Heterogeneous Electrode Models from Integrating Machine Learning and Atomistic Simulation. *Journal of Chemical Theory and Computation* **2023**, *19*, 5199–5209, PMID: 37477645.

86. Scalfi, L.; Dufils, T.; Reeves, K. G.; Rotenberg, B.; Salanne, M. A semiclassical Thomas–Fermi model to tune the metallicity of electrodes in molecular simulations. *The Journal of Chemical Physics* **2020**, *153*, 174704.

87. Scalfi, L.; Rotenberg, B. Microscopic origin of the effect of substrate metallicity on interfacial free energies. *Proceedings of the National Academy of Sciences* **2021**, *118*, e2108769118, Publisher: National Academy of Sciences Section: Physical Sciences.

88. Siepmann, J. I.; Sprik, M. Influence of surface topology and electrostatic potential on water/electrode systems. *J. Chem. Phys.* **1995**, *102*, 511–524.

89. Limmer, D. T.; Willard, A. P.; Madden, P.; Chandler, D. Hydration of metal surfaces can be dynamically heterogeneous and hydrophobic. *Proc. Natl. Acad. Sci. U.S.A.* **2013**, *110*, 4200–4205.

90. Dwelle, K. A.; Willard, A. P. Constant Potential, Electrochemically Active Boundary Conditions for Electrochemical Simulation. *J. Phys. Chem. C* **2019**, *123*, 24095–24103.

91. Zhao, R.; Remsing, R. C.; Weeks, J. D. Response Theory for Static and Dynamic Solvation of Ionic and Dipolar Solutes in Water. *Journal of Statistical Physics* **2020**, *180*, 721–738.

92. Limaye, A.; Suvlu, D.; Willard, A. P. Water molecules mute the dependence of the double-layer potential profile on ionic strength. *Faraday Discussions* **2023**, 10.1039.D3FD00114H.

93. Marin-Laflèche, A.; Haefele, M.; Scalfi, L.; Coretti, A.; Dufils, T.; Jeanmairet, G.; Reed, S. K.; Serva, A.; Berthin, R.; Bacon, C.; Bonella, S.; Rotenberg, B.; Mad-

den, P. A.; Salanne, M. MetalWalls: A classical molecular dynamics software dedicated to the simulation of electrochemical systems. *Journal of Open Source Software* **2020**, *5*, 2373.

94. Coretti, A.; Bacon, C.; Berthin, R.; Serva, A.; Scalfi, L.; Chubak, I.; Goloviznina, K.; Haefele, M.; Marin-Laflèche, A.; Rotenberg, B.; Bonella, S.; Salanne, M. MetalWalls: Simulating electrochemical interfaces between polarizable electrolytes and metallic electrodes. *The Journal* **2022**,

95. Thompson, A. P.; Aktulga, H. M.; Berger, R.; Bolintineanu, D. S.; Brown, W. M.; Crozier, P. S.; In 'T Veld, P. J.; Kohlmeyer, A.; Moore, S. G.; Nguyen, T. D.; Shan, R.; Stevens, M. J.; Tranchida, J.; Trott, C.; Plimpton, S. J. LAMMPS - a flexible simulation tool for particle-based materials modeling at the atomic, meso, and continuum scales. *Computer Physics Communications* **2022**, *271*, 108171.

96. Ahrens-Iwers, L. J. V.; Janssen, M.; Tee, S. R.; Meißner, R. H. ELECTRODE: An electrochemistry package for atomistic simulations. *The Journal of Chemical Physics* **2022**, *157*, 084801.

97. Berendsen, H. J. C.; Grigera, J. R.; Straatsma, T. P. The Missing Term in Effective Pair Potentials. *J. Phys. Chem.* **1987**, *91*, 6269–6271.

98. Dang, L. X. Mechanism and Thermodynamics of Ion Selectivity in Aqueous Solutions of 18-Crown-6 Ether: A Molecular Dynamics Study. *J. Am. Chem. Soc.* **1995**, *117*, 6954–6960.

99. Berg, A.; Peter, C.; Johnston, K. Evaluation and Optimization of Interface Force Fields for Water on Gold Surfaces. *Journal of Chemical Theory and Computation* **2017**, *13*, 5610–5623.

100. Tee, S. R.; Searles, D. J. Fully periodic, computationally efficient constant potential

molecular dynamics simulations of ionic liquid supercapacitors. *J. Chem. Phys.* **2022**, *156*.

101. Dufils, T.; Jeanmairet, G.; Rotenberg, B.; Sprik, M.; Salanne, M. Simulating Electrochemical Systems by Combining the Finite Field Method with a Constant Potential Electrode. *Phys. Rev. Lett.* **2019**, *123*, 195501.

102. Martyna, G. J.; Klein, M. L.; Tuckerman, M. E. Nosé-Hoover chains: the canonical ensemble via continuous dynamics. *J. Chem. Phys.* **1992**, *97*, 2635–2643.

103. Pireddu, G.; Fairchild, C. J.; Niblett, S. P.; Cox, S. J.; Rotenberg, B. Data related to the article "Impedance of nanocapacitors from molecular simulations to understand the dynamics of confined electrolytes". 2024; `https://doi.org/10.5281/zenodo.10958682`.

Supporting information for: Impedance of nanocapacitors from molecular simulations to understand the dynamics of confined electrolytes

Giovanni Pireddu,[†] Connie J. Fairchild,[‡] Samuel P. Niblett,[‡] Stephen J. Cox,[‡] and Benjamin Rotenberg[*,†,¶]

†*Sorbonne Université, CNRS, Physico-chimie des Électrolytes et Nanosystèmes Interfaciaux, PHENIX, F-75005 Paris*

‡*Yusuf Hamied Department of Chemistry, University of Cambridge, Cambridge CB2 1EW, United Kingdom*

¶*Réseau sur le Stockage Electrochimique de l'Energie (RS2E), FR CNRS 3459, 80039 Amiens Cedex, France*

E-mail: benjamin.rotenberg@sorbonne-universite.fr

Contents

1 Simulation details

1.1 Confined simulations

A summary of all simulation runs for the confined systems at equilibrium and non-equilibrium conditions are provided in tables S1 and S2. In the tables, we report the electrode surface area A_{el}, the distance between the electrodes d (obtained from equilibration at constant atmospheric pressure), the total number of ion pairs, the total number of water molecules, the number of replicas, and the simulation time considered for the production runs. For all the systems, we first run an equilibration simulation of 0.5 ns to find the equilibrium interelectrode distance d at constant atmospheric pressure. Then, we run at least 0.5 ns of dynamics in the NVT ensemble for a further equilibration. Replicas of the original systems are prepared by simulated annealing by performing 0.5 ns of dynamics at constant temperature $T = 500$ K followed by a 0.5 ns simulation at $T = 298$ K to re-equilibrate the system at the target temperature.

The uncertainty of the properties computed from simulation results was computed as the 95% confidence interval. In particular, in the case of equilibrium simulations at 0.1 M salt concentration, we considered each replica as an independent sample. In all the other cases, within each replica we split the simulation results into 5 samples (that are assumed to be uncorrelated) and calculate the confidence interval for each replica independently. Finally, the 'global' confidence interval for each system is obtained from error propagation of the mean among all the replicas. This procedure was designed to ensure that each individual sample would contain at least 10 ns of dynamics, which is beyond all the correlation times observed in this work.

For the non-equilibrium simulations, for each concentration a set of uncorrelated initial configurations were sampled from the equilibrium ensemble at $\Delta\Psi = 0\,\mathrm{V}$ (see Table S2). To obtain estimates of equilibrium values at $\Delta\Psi = 1\,\mathrm{V}$ [e.g., $\overline{Q}(\infty)$], further equilibrium simulations were performed for: 8 ns (0.1 M); 4.2 ns (0.5 M); 10 ns (1.0 M); 4.0 ns (1.5 M).

The uncertainty was computed as a 95 % confidence interval by treating each replica as an independent sample and by propagating the uncertainty from the equilibrium 1 V simulations.

1.2 Bulk simulations

In table S3, we report the simulation setups (volume of the simulation box V, number of ion pairs, number of water molecules) as well as the number of replicas and time windows considered for the bulk simulations. In all cases, prior to the production runs, we performed equilibration runs which included at least 1 ns of dynamics.

The uncertainty, calculated as the 95% confidence interval, was calculated by splitting each run into 5 samples, which are assumed to be uncorrelated.

2 Difference between QACFs for solutions and pure water

In order to analyse the influence of the presence of ions in the systems on the electrode charge dynamics, we subtracted the total charge autocorrelation functions sampled with pure water from the same quantity computed from finite salt concentration: $\langle \delta Q(0)\delta Q(t)\rangle_{\text{diff}} = \langle \delta Q(0)\delta Q(t)\rangle - \langle \delta Q(0)\delta Q(t)\rangle_{\text{w}}$, where $\langle \delta Q(0)\delta Q(t)\rangle_{\text{w}}$ is the QACF in the pure water case. Fig. S1 displays the QACF difference, normalised by the value at $t = 0$, for all the finite salt concentrations we considered. We then fitted all the QACF differences with exponential functions, in order to extract the characteristic times discussed in the main text.

3 Notes on decomposing the nonequilibirium polarization response

In Fig. 6 of the main article, we decomposed the polarization response into contributions from the solvent and ions. Here, we provide further details on how this decomposition relates to the equilibrium correlation functions at $\Delta\Psi = 0\,\mathrm{V}$. To begin, it is useful to briefly recap some of the key ideas underlying the statistical mechanics of linear response theory. Let us denote the Hamiltonian of the unperturbed system as $\mathcal{H}_0$. We then consider a perturbed Hamiltonian of the form

$$\mathcal{H}(t) = \mathcal{H}_0 - f(t)A(t) \tag{1}$$

where $A(t) \equiv A(\mathbf{r}^N(t))$ is an observable that couples to the driving force

$$f(t) = \begin{cases} 0, & t \leq 0, \\ f, & t > 0. \end{cases}$$

It can then be shown[1] that the nonequilibrium average of an observable $B(t)$ (for $t > 0$) is

$$\Delta\overline{B}(t) = \beta f \langle \delta B(t) \delta A(0) \rangle_0, \tag{2}$$

where $\Delta\overline{B}(t) = \overline{B}(t) - \overline{B}(0)$, and $\langle \cdot \rangle_0$ denotes an equilibrium average in the absence of the perturbation. Assuming $\langle \delta B(t \to \infty) \delta A(0) \rangle_0 = 0$, it can further be shown that

$$\frac{\overline{B}(t) - \overline{B}(\infty)}{\overline{B}(0) - \overline{B}(\infty)} = \frac{\langle \delta B(t) \delta A(0) \rangle_0}{\langle \delta B(0) \delta A(0) \rangle_0}. \tag{3}$$

For example, if we consider the response of the total charge on an electrode in response to a step change in the potential, we take $-f(t)A(t) = -\Delta\Psi(t)Q(t)$ and $B(t) = Q(t)$:

$$\frac{\overline{Q}(t) - \overline{Q}(\infty)}{\overline{Q}(0) - \overline{Q}(\infty)} = \frac{\langle \delta Q(t) \delta Q(0) \rangle_0}{\langle (\delta Q)^2 \rangle_0}. \tag{4}$$

Linear response is valid to the extent that Eq. 4 is satisfied (see Fig. 1(d) in the main text).

In the case of the electrolyte response, we instead consider $-fA(t) = -E_Q(t)M_{\rm tot}(t)$, where $E_Q(t) = -Q(t)/d$ is the instantaneous electric field established between electrodes by the charge $Q(t)$, and $M_{\rm tot}$ is the value of the total dipole moment of the solution along the surface normal (the field E_Q does not include the contribution from polarized electrolyte). It then follows that:

$$\frac{\overline{M}_{\rm tot}(t) - \overline{M}_{\rm tot}(\infty)}{\overline{M}_{\rm tot}(0) - \overline{M}_{\rm tot}(\infty)} = \frac{\langle \delta M_{\rm tot}(t) \delta M_{\rm tot}(0) \rangle_0}{\langle (\delta M_{\rm tot})^2 \rangle_0}, \tag{5}$$

$$\frac{\overline{M}_{\rm ion}(t) - \overline{M}_{\rm ion}(\infty)}{\overline{M}_{\rm tot}(0) - \overline{M}_{\rm tot}(\infty)} = \frac{\langle \delta M_{\rm ion}(t) \delta M_{\rm tot}(0) \rangle_0}{\langle (\delta M_{\rm tot})^2 \rangle_0}, \tag{6}$$

and,

$$\frac{\overline{M}_{\rm wat}(t) - \overline{M}_{\rm wat}(\infty)}{\overline{M}_{\rm tot}(0) - \overline{M}_{\rm tot}(\infty)} = \frac{\langle \delta M_{\rm wat}(t) \delta M_{\rm tot}(0) \rangle_0}{\langle (\delta M_{\rm tot})^2 \rangle_0}, \tag{7}$$

The sum of Eqs. 6 and 7 yields Eq. 5.

4 Dynamics of ionic polarization

Fig. S2 shows the mean squared displacement of the total ionic dipole moment $\mathbf{M}_{\rm ion}$ as a function of time, calculated from bulk simulations, for all the salt concentrations we considered. We fitted the simulation data with lines and extracted the ionic conductivity σ_0 using the Einstein-Helfand approach[2] (see the Methods section in the main text).

5 Bulk conductivity spectra

Fig. 3(b) of the main text displays the real part of the complex conductivity $\sigma(\omega)$ as a function of frequency, for all the salt concentrations we considered. It demonstrates the broad consistency between the low frequency behavior of $\sigma(\omega)$ obtained from Eq. 18 of the main paper, and the conductivity at $\omega = 0$ obtained with the Einstein-Helfand approach.

However, we note that results for 0.1 M are subject to large statistical uncertainty, and it is likely that we are yet to fully reach the low frequency regime in this case, nor can we rule out departure from the thin EDL limit ($\lambda_{\mathrm{D}} \ll d$).

Fig. S3 reports the imaginary part of $\sigma(\omega)$ as a function of frequency. For finite salt concentration, we found it beneficial for the analysis to remove the numerical noise present at low frequencies (shown in grey in Fig. S3). In particular, we exploit the fact that $\Im[\sigma(\omega \to 0)] \approx \omega\varepsilon_0(\varepsilon_{\mathrm{eff}} - 1)$,[3] where ε_0 is the vacuum permittivity and $\varepsilon_{\mathrm{eff}}$ is the effective static permittivity of the electrolyte solution. Indeed, in the low frequency part, besides the numerical noise, we observe this qualitative trend (see Fig. S4).

For the filtering procedure, we first fitted the MD data with $\omega\varepsilon_0(\varepsilon_{\mathrm{eff}} - 1)$, by tuning the effective permittivity $\varepsilon_{\mathrm{eff}}$. We obtained $\varepsilon_{\mathrm{eff}} = 61$, 56, 46, and 39, corresponding to 0.1, 0.5, 1.0, 1.5 M, respectively. The fact that $\varepsilon_{\mathrm{eff}}$ decreases with increasing salt concentration is in qualitative agreement with the notion of a dielectric decrement found both in simulations and experiments.[4,5] After fitting, the raw data is simply replaced by $\omega\varepsilon_0(\varepsilon_{\mathrm{eff}} - 1)$ for $\omega < 1.9 \times 10^{10}$ rad/s. We emphasize that this filtering procedure was only performed for finite salt concentrations; in the case of pure water, $\epsilon_{\mathrm{w}} = 70.7$ for SPC/E water was taken from the literature,[6] and found to describe the low frequency behavior of $\sigma(\omega)$ well.

6 Low frequency behavior of the bulk conductivity

We begin our discussion with the Green-Kubo expression for the bulk conductivity, Eq. 18 in the main text, which we repeat here for clarity:

$$\sigma(\omega) = \frac{\beta}{3V}\int_0^\infty \langle \delta\mathbf{J}(0)\cdot\delta\mathbf{J}(t)\rangle e^{-i\omega t}\mathrm{d}t \tag{8}$$

$$= \frac{\beta\langle(\delta J)^2\rangle}{3V}\int_0^\infty C_J(t)e^{-i\omega t}\mathrm{d}t, \tag{9}$$

where $C_J(t) = \langle \delta\mathbf{J}(0) \cdot \delta\mathbf{J}(t) \rangle / \langle (\delta J)^2 \rangle$. Expanding the exponential,

$$\frac{\beta \langle (\delta J)^2 \rangle}{3V} \int_0^\infty C_J(t) \left(1 - i\omega t - \frac{\omega^2 t^2}{2} - \frac{i\omega^3 t^3}{6} + \dots \right) \mathrm{d}t, \tag{10}$$

defining,

$$\sigma_0 = \frac{\beta \langle (\delta J)^2 \rangle}{3V} \int_0^\infty C_J(t) \mathrm{d}t, \tag{11}$$

$$\sigma_1 = -\frac{\beta \langle (\delta J)^2 \rangle}{3V} \int_0^\infty t C_J(t) \mathrm{d}t, \tag{12}$$

$$\sigma_2 = -\frac{\beta \langle (\delta J)^2 \rangle}{6V} \int_0^\infty t^2 C_J(t) \mathrm{d}t, \tag{13}$$

$$\dots, \tag{14}$$

and collecting real and imaginary parts, we arrive at Eqs. 5 and 6 in the main text:

$$\Re[\sigma(\omega)] = \sigma_0 + \sigma_2 \omega^2 + \sigma_4 \omega^4 + \dots, \tag{15}$$

$$\Im[\sigma(\omega)] = \sigma_1 \omega + \sigma_3 \omega^3 \dots \tag{16}$$

with $\sigma_1 = \epsilon_0(\epsilon_{\text{eff}} - 1)$. For the practical purposes of this work, we only need to extract numerical values for coefficients up to and including σ_2. We obtain σ_1 from $\Im[\sigma(\omega)]$ as described in the previous section. The remaining coefficients σ_0 and σ_2 are obtained by fitting Eq. 15 directly to simulation data for $\Re[\sigma(\omega)]$ (see Fig. S5). For pure water, $\sigma_0 = 0$ and $\sigma_1 = \varepsilon_0(\varepsilon_{\text{w}} - 1)$ with the known value of the SPC/E water permittivity, so that only σ_2 is fitted, resulting in $\sigma_2 \approx 6.4\,10^{-21}\ \mathrm{S\,s^2/m}$. This corresponds (see Eqs. 32-33 below) to a Debye relaxation time $\sigma_2/\sigma_1 = \tau_{\text{w,bulk}} \approx 10$ ps, which is consistent with the value for bulk water (9 ps).

7 Low frequency behavior of the bulk impedance

As described in the main text, the bulk impedance is given by

$$Z_{\mathrm{bulk}}(\omega) = \frac{d_{\mathrm{DDS}}}{A_{\mathrm{el}}} \frac{1}{\sigma(\omega)}, \tag{17}$$

with real and imaginary parts

$$\Re[Z_{\mathrm{bulk}}(\omega)] = \frac{\Re[\sigma(\omega)]}{\Re[\sigma(\omega)]^2 + \Im[\sigma(\omega)]^2} \frac{d_{\mathrm{DDS}}}{A_{\mathrm{el}}}, \tag{18}$$

and

$$\Im[Z_{\mathrm{bulk}}(\omega)] = -\frac{\Im[\sigma(\omega)]}{\Re[\sigma(\omega)]^2 + \Im[\sigma(\omega)]^2} \frac{d_{\mathrm{DDS}}}{A_{\mathrm{el}}}, \tag{19}$$

respectively. The MD results for real and imaginary parts of Z_{bulk} are reported as a function of frequency in Figs. S6 and S7, respectively. In Fig. S6 we note the striking similarity of $\Re[Z_{\mathrm{bulk}}(\omega)]$ with the real part of the total impedance $Z(\omega)$ shown in Fig. 2 of the main text, across all frequencies we have investigated. We now consider the low frequency behavior of $\Re[Z_{\mathrm{bulk}}]$ for the case $\sigma_0 > 0$, i.e., finite ion concentration. Substituting in the low-frequency expansions of $\sigma(\omega)$ (Eqs. 15 and 16):

$$\Re[Z_{\mathrm{bulk}}(\omega \to 0)] = \frac{\sigma_0 + \sigma_2\omega^2}{(\sigma_0 + \sigma_2\omega^2)^2 + (\sigma_1\omega + \sigma_3\omega^3)^2} \frac{d_{\mathrm{DDS}}}{A_{\mathrm{el}}} \tag{20}$$

$$= \frac{\sigma_0 + \sigma_2\omega^2}{\sigma_0^2\left[1 + (2\sigma_0\sigma_2 + \sigma_1^2)\omega^2/\sigma_0^2 + \mathcal{O}(\omega^4)\right]} \frac{d_{\mathrm{DDS}}}{A_{\mathrm{el}}}, \tag{21}$$

$$\approx \frac{1}{\sigma_0}\left[1 - \left(\frac{\sigma_0\sigma_2 + \sigma_1^2}{\sigma_0^2}\right)\omega^2\right] \frac{d_{\mathrm{DDS}}}{A_{\mathrm{el}}}. \tag{22}$$

This is Eq. 9 in the main article. A comparison between simulation data and Eq. 22 with the parameters fitted on the bulk conductivity is shown in Fig. S6. In general, we find a good agreement between simulation data and this quadratic form at low frequencies. The low-

frequency extrapolations are also in broadly good agreement with the resistivity predicted by the Einstein-Helfand approach (see also Table S4). Given the similarity between the bulk and confined impedance (shown in Figs. S6 and S8, respectively), we also use a two-parameter fit (i.e., the intercept and coefficient of ω^2) to obtain the cell resistance $R = \Re[Z(\omega \to 0)]$ (see Table S4). [In principle, we could also use such a two-parameter fit to obtain new estimates for σ_0 and σ_2, while using the value of σ_1 from $\Im[Z_{\text{bulk}}(\omega \to 0)]$; however, as $\sigma_0\sigma_2 \ll \sigma_1^2$ (see Table S5), we have found this numerically challenging.] In general, we find a good agreement between the fitted parameters, except for the 0.1 M case.

In the main text, we also discuss the Nernst-Einstein (NE) approximation of the static conductivity:

$$\sigma_0^{\text{NE}} = \frac{e^2}{k_{\text{B}}T}\left(c_{\text{Na}}D_{\text{Na}}z_{\text{Na}}^2 + c_{\text{Cl}}D_{\text{Cl}}z_{\text{Cl}}^2\right) = \frac{2}{k_{\text{B}}T}FeDC_{\text{NaCl}}, \tag{23}$$

where F is the Faraday constant, e is the electron charge, $D = 1.41\times10^{-9}$ m^2/s is the average diffusion coefficient of Na and Cl ions, and C_{NaCl} is the NaCl concentration in units of moles m^{-3}. The NE resistivity and corresponding resistance are calculated as $\rho_{\text{NE}} = 1/\sigma_0^{\text{NE}}$ and $R_{\text{NE}} = \rho_{\text{NE}}d/A_{\text{el}}$, respectively.

We now consider the case of dielectrics, $\sigma_0 = 0$, e.g., pure water,

$$\Re[Z_{\text{w,bulk}}(\omega \to 0)] = \frac{\sigma_2\omega^2 + \sigma_4\omega^4}{(\sigma_2\omega^2 + \sigma_4\omega^4)^2 + (\sigma_1\omega + \sigma_3\omega^3)^2}\frac{d_{\text{DDS}}}{A_{\text{el}}}, \tag{24}$$

$$= \frac{\sigma_2 + \sigma_4\omega^2}{\sigma_1^2 + (\sigma_2^2 + 2\sigma_1\sigma_3)\omega^2 + \mathcal{O}(\omega^4)}\frac{d_{\text{DDS}}}{A_{\text{el}}}, \tag{25}$$

$$\approx \frac{\sigma_2}{\sigma_1^2}\left[1 - \left(\frac{\sigma_2^2 + 2\sigma_1\sigma_3}{\sigma_1^2} - \frac{\sigma_4}{\sigma_2}\right)\omega^2\right]\frac{d_{\text{DDS}}}{A_{\text{el}}}. \tag{26}$$

This is Eq. 10 in the main article. Unlike the case of electrolytes, we see that the coefficient of ω^2 depends upon all non-zero coefficients of the bulk conductivity up to σ_4; obtaining reliable estimates for these higher-order coefficients is challenging. Instead, we simply perform a two-parameter fit (i.e., the intercept and coefficient of ω^2) of Eq. 26 to our simulation data. As

shown in Fig. S6, such a quadratic form describes the simulation data well at sufficiently low frequency.

We now consider the low frequency behavior of $\Im[Z_{\text{bulk}}]$ (Eq. 19). Following a similar procedure as we did for $\Re[Z_{\text{bulk}}(\omega)]$, we find

$$\Im[Z_{\text{bulk}}(\omega \to 0)] = -\frac{\sigma_1 \omega}{\sigma_0^2 + (2\sigma_0\sigma_2 + \sigma_1^2)\omega^2} \frac{d_{\text{DDS}}}{A_{\text{el}}}, \tag{27}$$

where again we note that $\sigma_1 = \varepsilon_0(\varepsilon_{\text{eff}} - 1)$. This is Eq. 7 in the main article. For finite salt concentration, $\sigma_0 > 0$, Eq. 27 predicts a minimum at $\sigma_0/\sqrt{2\sigma_0\sigma_2 + \sigma_1^2}$. For dielectric systems such as pure water, $\sigma_0 = 0$, we instead obtain a qualitatively different behavior:

$$\Im[Z_{\text{w,bulk}}(\omega \to 0)] = -\frac{1}{\omega\sigma_1} = -\frac{1}{\omega\varepsilon_0(\varepsilon_{\text{w}} - 1)} \frac{d_{\text{DDS}}}{A_{\text{el}}}. \tag{28}$$

Fig. S7 shows that Eqs. 27 and 28 capture very well the trends observed from MD results for all systems we have investigated. The results for 0.1 M are subject to large statistical uncertainty, and it is also likely that we have not fully reached the low frequency limit in our simulations.

Finally, in the specific case of the Debye relaxation model for the solvent polarization, the frequency-dependent permittivity is

$$\varepsilon_{\text{w}}(\omega) = 1 + \frac{\varepsilon_{\text{w}} - 1}{1 + i\omega\tau_{\text{w,bulk}}} \tag{29}$$

where $\tau_{\text{w}} \approx 9$ ps for bulk SPC/E water, so that the conductivity reads:

$$\sigma(\omega) = i\omega\varepsilon_0[\varepsilon_{\text{w}}(\omega) - 1] = \frac{i\omega\varepsilon_0[\varepsilon_{\text{w}} - 1]}{1 + i\omega\tau_{\text{w,bulk}}} \approx i\omega\varepsilon_0[\varepsilon_{\text{w}} - 1] + \varepsilon_0[\varepsilon_{\text{w}} - 1]\tau_{\text{w,bulk}}\omega^2 + ... \tag{30}$$

Comparing with Eqs. 5 and 6 from the main text, this provides:

$$\sigma_0 = 0 \tag{31}$$

$$\sigma_1 = \varepsilon_0[\varepsilon_{\mathrm{w}} - 1] \tag{32}$$

$$\sigma_2 = \varepsilon_0[\varepsilon_{\mathrm{w}} - 1]\tau_{\mathrm{w,bulk}}\,. \tag{33}$$

In particular, with this model we expect $\sigma_2/\sigma_1 = \tau_{\mathrm{w,bulk}}$.

8 Effect of interelectrode distance

As shown in the main text (Section 1B), to the extent that C_{diff} is independent of d, we can use the simple EC model to predict $Z(\omega)$ for different system sizes. Here we provide additional data on the effect of the interelectrode distance, for d = 2.56, 5.07, 9.80, and 19.84 nm. Fig. S9(a) shows a direct comparison of C_{diff} (scaled by the lateral area A_{el} of the electrodes) as a function of d, for gold nanocapacitors with pure water and 1.0 M NaCl solutions. For pure water, C_{diff} decreases with increasing d, in qualitative agreement with what is expected from macroscopic theories of pure dielectrics, $C = \varepsilon_0\varepsilon_w A_{el}/d$ (see Ref. 7 for more discussion of this case). In contrast, at 1.0 M C_{diff} only mildly depends on d. This result is in qualitative agreement with mean field theories, which predict that, for finite salt concentrations, the differential capacitance is expected to depend exclusively on the screening length λ_{D} (see *e.g.* Eq. 2 of the main text, despite its limitations at such a concentration) in the limit of large d.

Fig. S9(b) reports the QACF at $\Delta\Psi$ = 0 V, which quantifies the electrode charge dynamics, for all the considered values of d. In all cases, we recognize the same qualitative features discussed in the main text for d = 5.07 nm (see Fig. 1(c) of the main text). The short time oscillations, corresponding to the high frequency peak in the admittance (see Fig. 3(a) of the main text), are very similar to that observed for pure water. As described

in Ref. 7, they can be ascribed to water libration of water molecules that reside beyond the adlayer (formed by water molecules in contact with the surface), even though the latter also contribute to a lesser extent, with a relative weight which depends on the distance between the electrodes. As the inter-electrode distance d increases, these oscillations appear to be progressively attenuated due to the increased dissipation also reflected in the larger real part of the impedance.[7] In the presence of ions, we further observe that both the characteristic time and the amplitude of the additional slow relaxation mode increase with d, as described in Section 1B of the main text.

9 Fitting τ_{Q}

As discussed in the main text, a comparison between characteristic times and MD results showed that $\tau_{\mathrm{mix}} = \lambda_{\mathrm{D}}(d - 2\lambda_{\mathrm{D}})/2D$, better than the Debye time $\tau_{\mathrm{D}} = \lambda_{\mathrm{D}}^2/D$, can qualitatively describe the scaling of the overall relaxation time τ_{Q} with salt concentration. In this section, we also consider τ_{JB} which is the more general solution to the electrokinetics of charging in capacitors obtained within the Debye-Falkenhagen approximation.[8] To highlight the qualitative match between analytical theories and MD data, we fit scaling factors (resp. γ_1, γ_2, γ_3) that multiply the time scales (resp. τ_{Debye}, τ_{mix}, τ_{JB}) to fit the behaviour of τ_{Q} with concentration.

The results of the fitting procedure are shown in Fig. S10. We observe that τ_{Debye} describes the MD data only in a qualitative way, whereas τ_{mix} and τ_{JB} fit well the simulation data with similar accuracy. The optimal scaling parameters are $\gamma_1 = 0.102$, $\gamma_2 = 0.036$ and $\gamma_3 = 0.032$.

10 Windowing

As reported in a previous work,[7] the autocorrelation functions estimated from molecular simulations are affected by numerical noise at large times. This negatively impacts the quality of the numerical Fourier-Laplace transforms used in this work, especially at high frequencies.

To mitigate this effect, we multiply the autocorrelation functions by a windowing function W with the following form

$$W(\epsilon, \tau) = \frac{e^{-\epsilon\tau} + 1}{e^{\epsilon(t-\tau)} + 1}, \tag{34}$$

where ϵ and τ are adjustable parameters that are tuned by hand for each system independently. The tuning is done with the goal of removing the long-time noise while preserving the overall shape of the original functions.

Direct comparisons of the original functions, their windowed version, and the window functions are shown in Figs. S11 and S12 for the confined systems, and in Figs. S13 for the bulk water system.

For pure water (shown in Fig. S13), 1.0 M and 1.5 M systems, we used window functions with $\epsilon = 18.9 \times 10^9$ s^{-1} and $\tau = 0.1 \times 10^{-9}$ s. For the 0.1 M and 0.5 M cases we used the same value for ϵ, but a higher value for τ (0.2×10^{-9}), as required by the slower decay at long times.

11 Figures

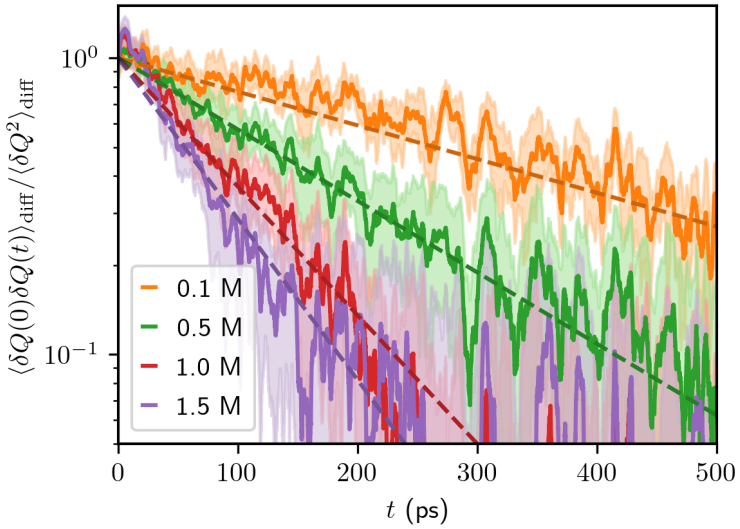

Figure S1: Difference between total charge autocorrelation functions at finite salt concentrations with respect to the same quantity computed for pure water systems[7] ($\langle \delta Q(0)\delta Q(t)\rangle_{\mathrm{diff}}$, solid lines), as a function of time. The results are normalized with respect to the value at $t = 0$ ($\langle \delta Q^2\rangle_{\mathrm{diff}}$). All the curves are fitted with exponential functions (dashed lines).

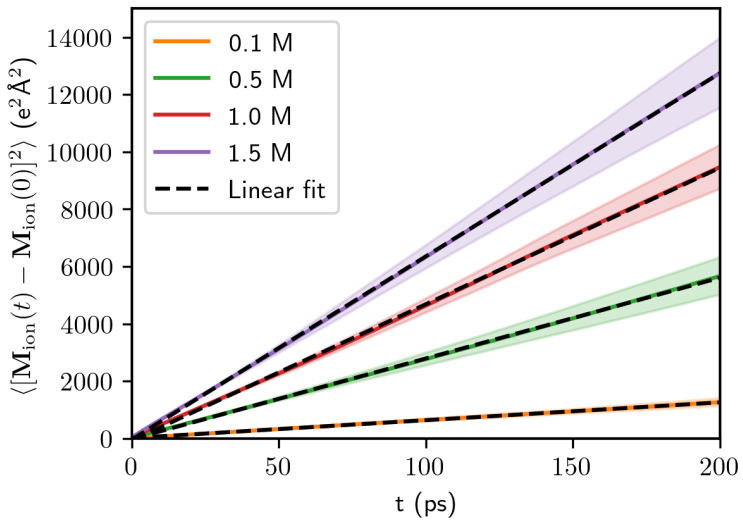

Figure S2: Mean squared displacement of the total ionic dipole moment $\mathbf{M}_{\rm ion}$ as a function of time, for all the salt concentration we considered (solid lines). The simulation data are fitted with linear functions (dashed lines).

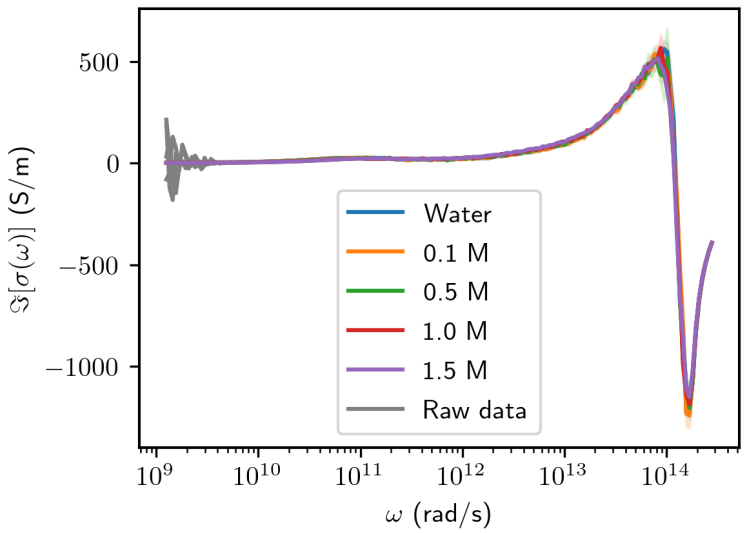

Figure S3: Imaginary part of conductivity computed from bulk simulations $\Im[\sigma(\omega)]$, shown as solid lines as a function of frequency. The colored lines represent the raw data set, whereas the colored lines represent the dataset upon filtering (see text).

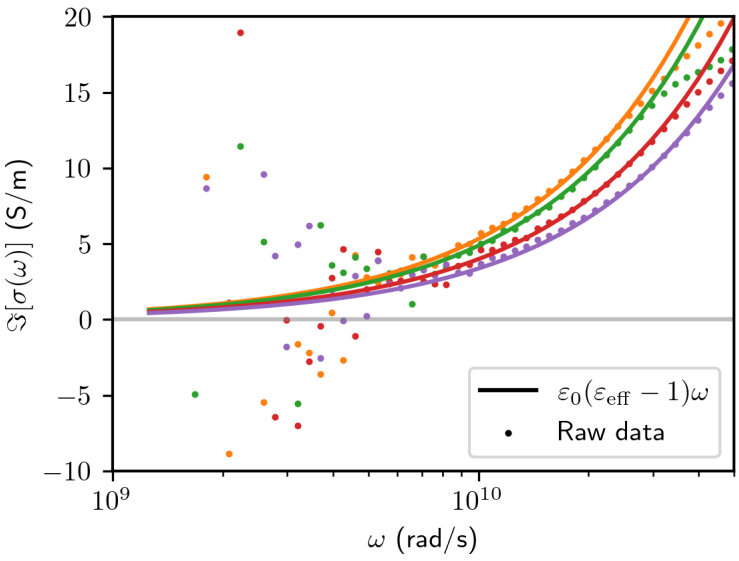

Figure S4: Imaginary part of conductivity computed from bulk simulations $\sigma(\omega)$ as a function of frequency. The dots correspond to the raw data ($\Im[\sigma(\omega)]$ computed directly from MD results), while the solid lines represent $\sigma_1\omega = \varepsilon_0(\varepsilon_{\text{eff}} - 1)\omega$ functions fitted to the MD data, except for pure water where we use the permittivity of the SPC/E model[6]. The colors are coded as in Fig. S3. Namely, 0.1, 0.5, 1.0, and 1.5 M are represented with orange, green, red, and violet colors, respectively.

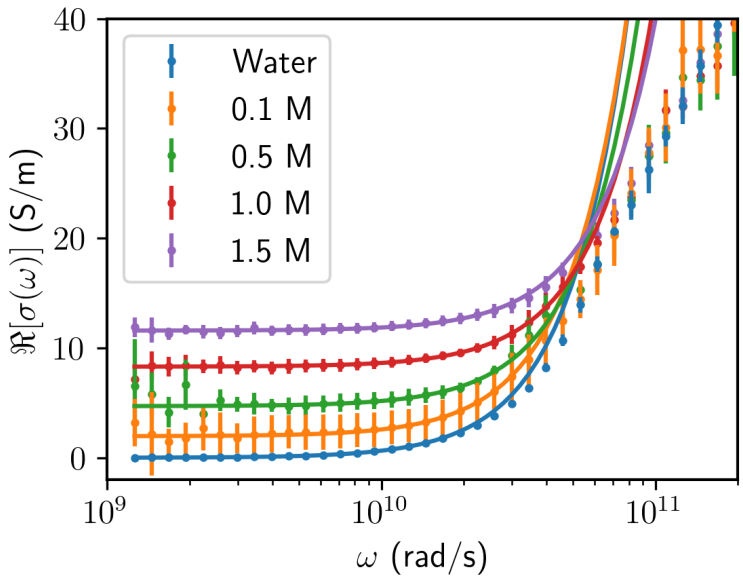

Figure S5: Real part of conductivity computed from bulk simulations $\sigma(\omega)$ as a function of frequency. The dots correspond to MD results, while the fits (Eq. 15) are represented with solid lines. The corresponding fitting parameters σ_0 and σ_2 can be found in Table S5 (for water only σ_2 is fitted since $\sigma_0 = 0$).

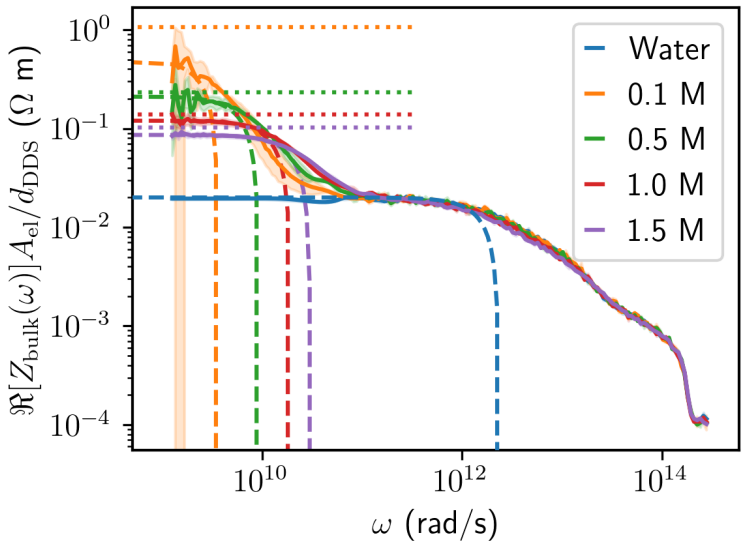

Figure S6: Real part of bulk impedance Z_{bulk} as a function of frequency for different NaCl concentrations. The horizontal dotted lines correspond to the Einstein-Helfand estimate of the bulk resistance $R^{EH}_{\mathrm{bulk}} = d/\sigma_0^{\mathrm{EH}} A_{\mathrm{el}}$. For the electrolytes, the dashed lines are predictions from Eq. 22 using the values of parameters σ_i obtained by fitting $\Re[\sigma(\omega)]$ and $\Im[\sigma(\omega)]$ (see text and Figs. S4 and S5). For water, the dashed line is a quadratic fit.

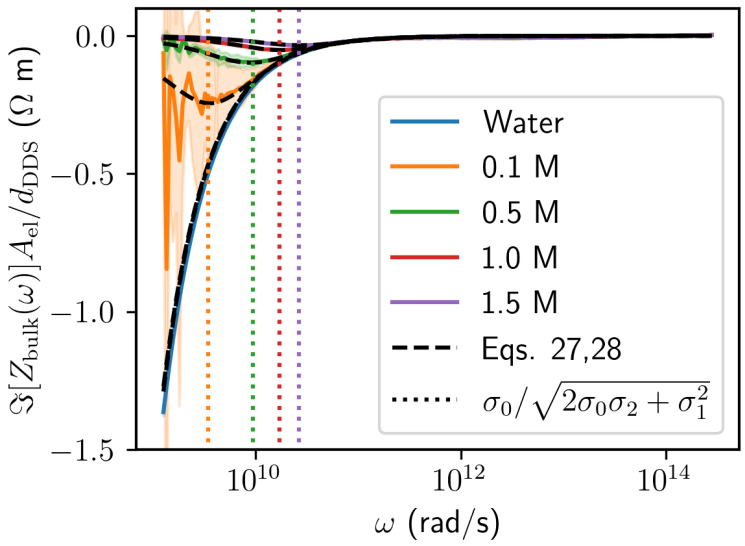

Figure S7: Imaginary part of bulk impedance Z_{bulk} as a function of frequency. The MD results (solid lines) are compared with the low-frequency limit of Eq. 19 (see Eq. 27), using the parameters σ_i obtained by fitting $\Re[\sigma(\omega)]$ and $\Im[\sigma(\omega)]$ (see text and Figs. S4 and S5), represented as black dashed lines. For water, the black dashed line corresponds to Eq. 28 using the bulk permittivity of the SPC/E water model. The vertical dotted lines indicate the location of the local minima of Eq. 27.

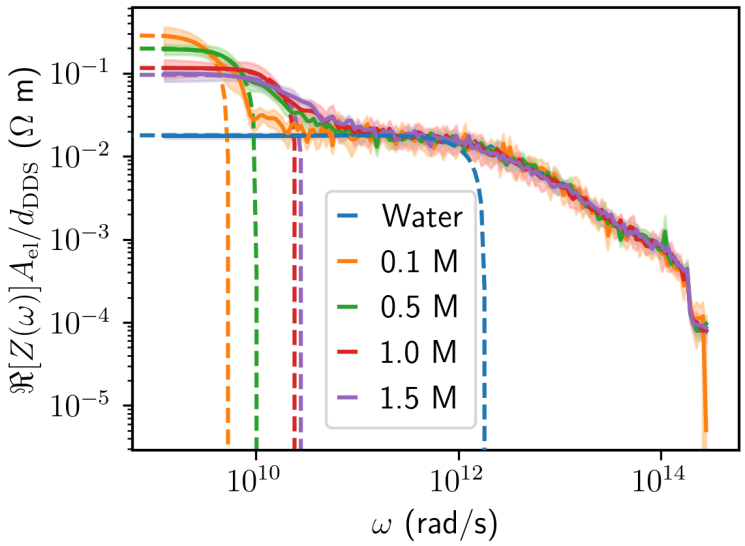

Figure S8: Real part of the cell impedance Z as a function of frequency for different NaCl concentrations. The dashed lines represent quadratic fits (following the form of Eq. 22, even though the bulk parameters are not used), from which we extract the plateau value for $R = Z(\omega \to 0)$.

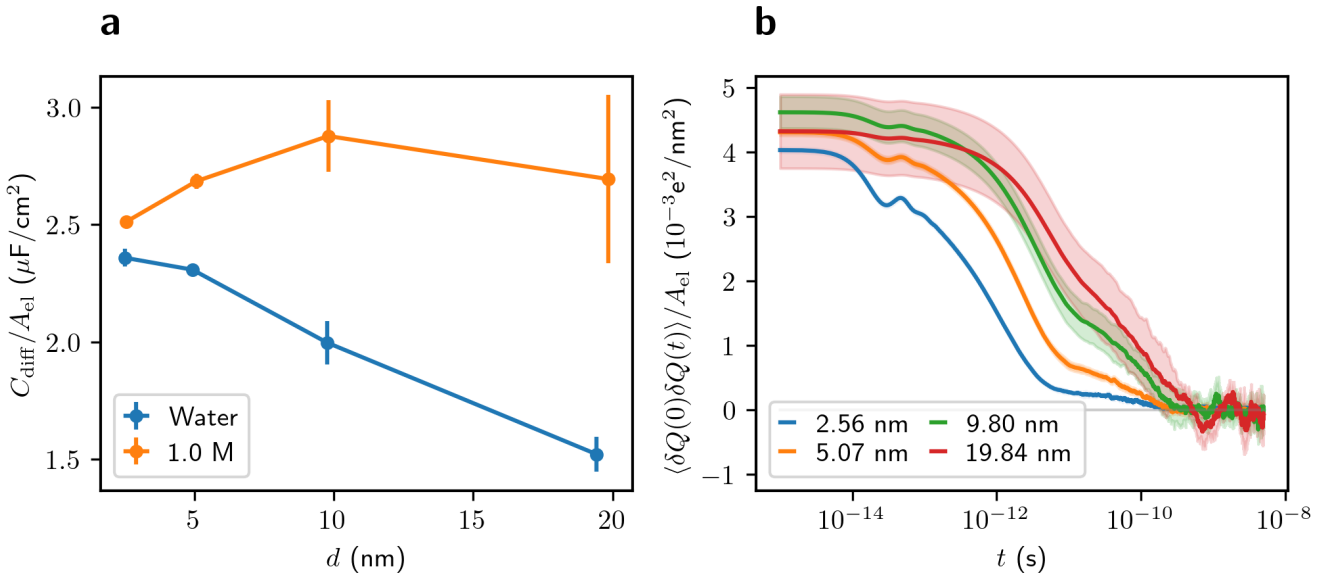

Figure S9: (a) Differential capacitance C_{diff} divided by the lateral area of the electrodes, A_{el}, as a function of d for pure water[7] (blue) and 1.0 M NaCl aqueous solution (orange). (b) Electrode charge auto-correlation function, $\langle\delta Q(0)\delta Q(t)\rangle$, divided by A_{el} as a function of t, for all the considered inter-electrode distances.

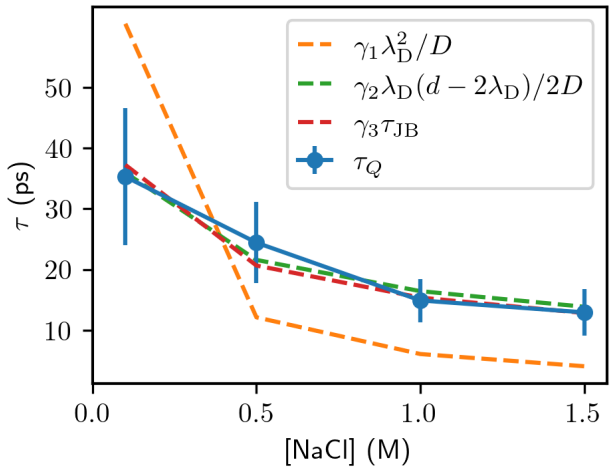

Figure S10: Comparison between the characteristic time τ_Q computed from the integral of the QACFs (symbols) and scaled formulas from analytical theories (dashed lines). The optimal parameters $\gamma_1 = 0.102$, $\gamma_2 = 0.036$ and $\gamma_3 = 0.032$ were obtained by fitting to the simulation data.

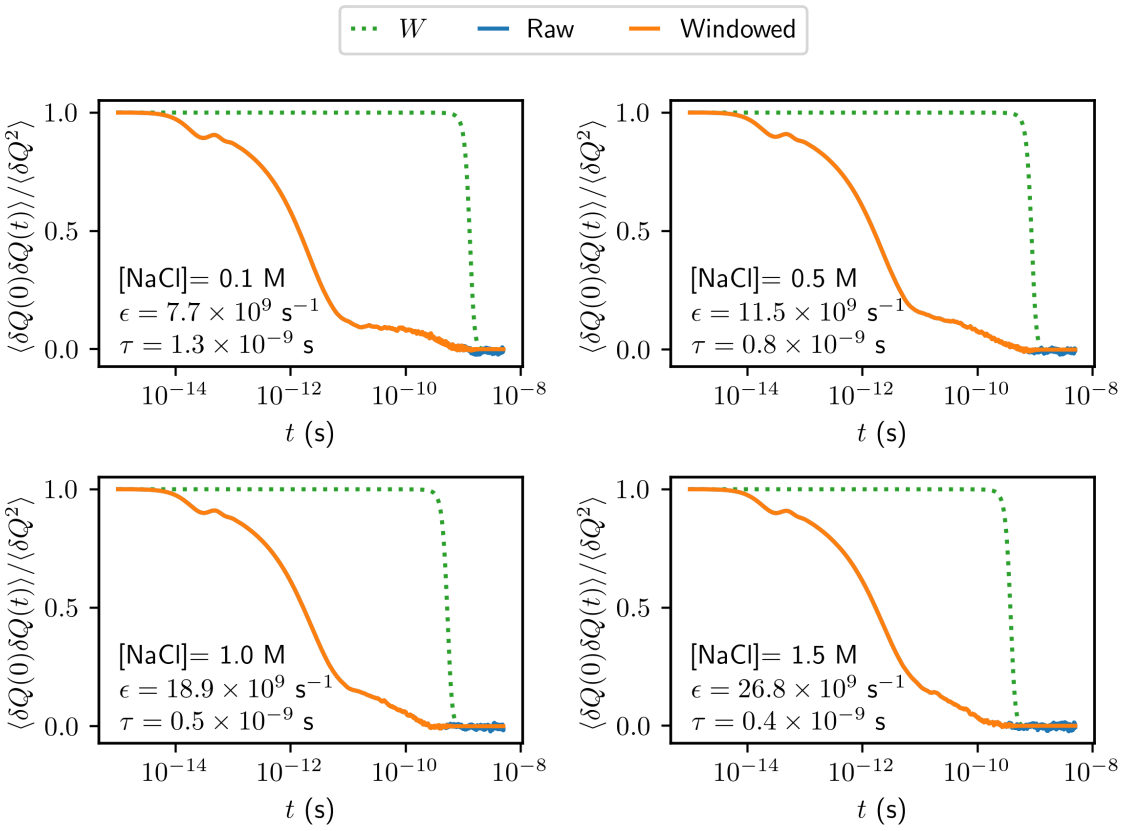

Figure S11: Comparison between the window functions W (see Eq. 34), the raw total charge autocorrelation functions as calculated from the MD simulations, and the same after being multiplied by W. Each plot reports the salt concentration, and the parameters ϵ and τ used for the window function.

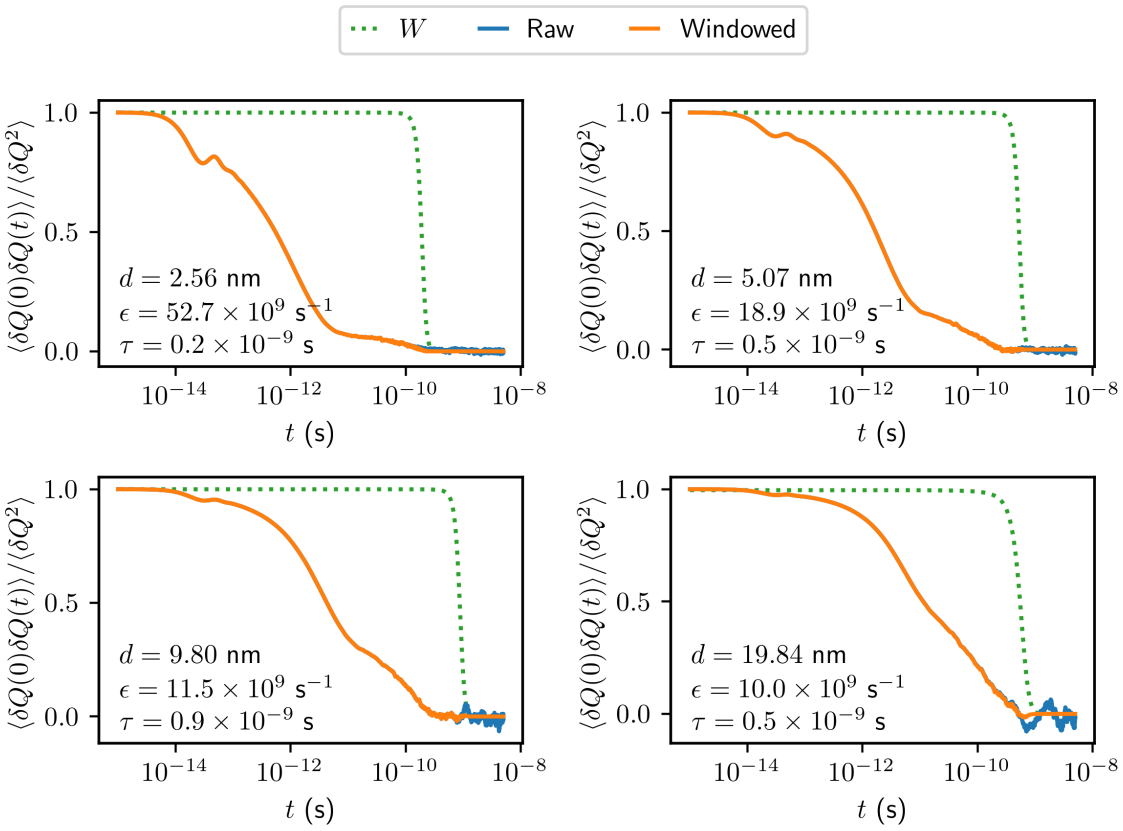

Figure S12: Comparison between the window functions W (see Eq. 34), the raw total charge autocorrelation functions as calculated from the MD simulations, and the same after being multiplied by W. Each plot reports the interelectrode distance d, and the parameters ϵ and τ used for the window function.

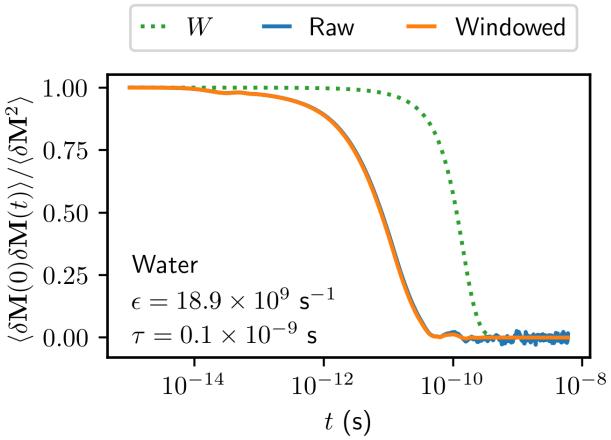

Figure S13: Comparison between the window function W (see Eq. 34), the raw total dipole moment autocorrelation function as calculated from the MD simulations of the bulk water system, and the same after being multiplied by W.

12 Tables

Table S1: Confined equilibrium simulations

[NaCl](M)	A_{el} (Å^2)	d (Å)	ion pairs	water molecules	replicas	simulation time (ns)
0.0*	1341.75*	49.4*	0*	2160*	1*	50*
0.1	5367.00	49.3	16	8640	10	12
0.5	1341.75	49.8	20	2160	3	50
1.0	1341.75	25.6	19	1080	1	50
1.0	1341.75	50.6	39	2160	3	50
1.0	1341.75	98.0	78	4320	1	50
1.0	1341.75	198.4	156	8640	1	50
1.5	1341.75	51.0	59	2160	2	50

* Simulation results from Ref. 7.

Table S2: Confined non-equilibrium simulations

[NaCl](M)	A_{el} (Å^2)	d (Å)	ion pairs	water molecules	replicas	simulation time (ns)
0.1	5367.00	49.3	16	8640	20	1.0
0.5	1341.75	49.8	20	2160	10	1.0
1.0	1341.75	50.6	39	2160	40	1.0
1.5	1341.75	51.0	59	2160	10	1.0

Table S3: Bulk equilibrium simulations

[NaCl](M)	V (Å^3)	ion pairs	water molecules	replicas	simulation time (ns)
0.0	68468.11	0	2160	1	50
0.1	68468.11	4	2160	1	50
0.5	68468.11	20	2160	1	50
1.0	68468.11	39	2160	1	50
1.5	68468.11	59	2160	1	50

Table S4: Bulk resistivity values $\rho_{\text{bulk}} = 1/\sigma_0$ for each concentration, obtained by the Einstein-Helfand (EH) or Green-Kubo (GK) methods or predicted by the Nernst-Einstein (NE) equation. The results are compared with the resistivity of the confined system for $d = 5.07$ nm, obtained from the cell resistance as $\rho = RA_{\text{el}}/d_{\text{DDS}}$.

[NaCl](M)	ρ_{bulk}^{EH} (Ωm)	ρ_{bulk}^{GK} (Ωm)	ρ_{bulk}^{NE} (Ωm)	$RA_{\text{el}}/d_{\text{DDS}}$ (Ωm)
0.1	1.06 ± 0.11	0.510 ± 0.075	0.94	0.296 ± 0.030
0.5	0.23 ± 0.03	0.213 ± 0.007	0.19	0.200 ± 0.007
1.0	0.14 ± 0.01	0.120 ± 0.002	0.09	0.116 ± 0.004
1.5	0.10 ± 0.01	0.086 ± 0.001	0.06	0.096 ± 0.003

Table S5: Optimal values for σ_0 and σ_2 resulting form the fit of the conductivity $\Re[\sigma(\omega)]$ of bulk electrolytes (see Eq. 15) and Fig. S5.

[NaCl](M)	σ_0 (S/m)	σ_2 ($\mathrm{S\,s^2/m}$)
0.1	2.0 ± 0.3	6.1E-21 ± 1E-21
0.5	4.7 ± 0.2	4.7E-21 ± 4E-22
1.0	8.3 ± 0.1	3.4E-21 ± 4E-22
1.5	11.6 ± 0.1	2.8E-21 ± 4E-22

References

1. Chandler, D. *Introduction to Modern Statistical Mechanics*; Oxford University Press, 1987.

2. Schröder, C.; Haberler, M.; Steinhauser, O. On the computation and contribution of conductivity in molecular ionic liquids. *J. Chem. Phys.* **2008**, *128*, 134501.

3. Hansen, J.-P.; McDonald, I. *Theory of simple liquids*, 4th ed.; Academic Press, 1986.

4. Kalcher, I.; Dzubiella, J. Structure-thermodynamics relation of electrolyte solutions. *The Journal of Chemical Physics* **2009**, *130*, 134507.

5. Rinne, K. F.; Gekle, S.; Netz, R. R. Dissecting ion-specific dielectric spectra of sodium-halide solutions into solvation water and ionic contributions. *The Journal of Chemical Physics* **2014**, *141*, 214502.

6. Rami Reddy, M.; Berkowitz, M. The dielectric constant of SPC/E water. *Chemical Physics Letters* **1989**, *155*, 173–176.

7. Pireddu, G.; Rotenberg, B. Frequency-Dependent Impedance of Nanocapacitors from Electrode Charge Fluctuations as a Probe of Electrolyte Dynamics. *Phys. Rev. Lett.* **2023**, *130*, 098001.

8. Janssen, M.; Bier, M. Transient Dynamics of Electric Double-Layer Capacitors: Exact Expressions Within the Debye-Falkenhagen Approximation. *Phys. Rev. E* **2018**, *97*, 052616.